Naval Information Warfare Center
PACIFIC

TECHNICAL REPORT 3232
APRIL 2021

# Physics-Based Splines Interpolating Electric-Field Measurements

Jeffery C. Allen
David R. Hilton
Kristopher R. Buchanan
John H. Meloling

**NIWC Pacific**



Naval Information Warfare Center Pacific (NIWC Pacific)
San Diego, CA 92152-5001

This page is intentionally blank.

TECHNICAL REPORT 3232
APRIL 2021

# Physics-Based Splines Interpolating Electric-Field Measurements

Jeffery C. Allen
David R. Hilton
Kristopher R. Buchanan
John H. Meloling
**NIWC Pacific**



**Administrative Notes:**
This report was approved through the Release of Scientific and Technical Information (RSTI) process in June 2020 and formally published in the Defense Technical Information Center (DTIC) in April 2021.

NIWC Pacific
San Diego, CA 92152-5001

**NIWC Pacific**
**San Diego, California 92152-5001**

A. D. Gainer, CAPT, USN
Commanding Officer

W. R. Bonwit
Executive Director

## ADMINISTRATIVE INFORMATION

The work described in this report was performed by Code 75250 of the Electromagnetic & Advanced Technology Division, Naval Information Warfare Center Pacific (NIWC Pacific), San Diego, CA. Evangela M. Waite (Part of NAVSEA 05H) provided funding for this Basic Applied Research project. Further assistance was provided by the Chief of Naval Operations for Information Dominance/Director of Naval Intelligence (OPNAV N2/N6) and Naval Sea Systems Command (NAVSEA) Code 05W.

Released by
Jodi McGee, Division Head
Electromagnetic & Advanced Technology Division

Under authority of
Carly Jackson, Department Head
Cyber/S&T Department



Edited by:
Robert J. Price

# EXECUTIVE SUMMARY

Mitigating Electro-Magnetic Interference (EMI) is a long-term engineering problem for shipboard RF systems [15], [14]. Measuring the electric field is basic to EMI mitigation. This report analyses electric-field measurements taken on the flight deck of a carrier. These electric field is sparsely sampled at selected locations on the flight deck. Interpolation schemes "fill in" the electric field between sample points. The quality of these interpolated electric fields is the "object of discussion" of this report.

Standard splines do not encode the physics of the problem—that the electric field in free space has zero divergence. This report develops a class of splines with zero divergence. Comparisons between these divergence-free splines and standard splines demonstrates enforcing zero divergence improves the quality of the spline—fewer sample points are required to recover the electric field with greater accuracy than the standard splines.

Applying a divergence-free spline to these flight-deck measurements requires a hybrid approach because only the electric field magnitude was measured. The hybrid approach exploits knowledge of the physical measurement to constrain the divergence-free splines to interpolate the amplitude at each sample point while leaving the phases as free variables at each sample point. The phases are optimized to approximate the splined electric-field magnitude. Consequently, the hybrid approach produces a divergence-free spline that matches the measured amplitude at each sample point and is a best approximation to the standard spline.

Reducing the sampling density means these divergence-free splines support scanning electric fields over physically large areas, including

- Regions above flight decks.
- Shipboard HF/VHF/UHF antenna patterns,
- VLF antenna patterns.

The approach for all these measurements employs a UAV to fly through a relevant part of the electric field. The UAV produces a fast sampling of the 3-D electric field for interpolation by the divergence-free splines. The final section of this report details these applications.

This page is intentionally blank.

# CONTENTS



# APPENDICES

# FIGURES

This page is intentionally blank.

# 1. SPLINES AND PHYSICS-BASED SPLINES

The standard splines, such as the cubic spline, are mathematical functions that interpolate sampled data and "fill-in" the data between the sample points. Although standard splines are smooth functions that match the measurements at each sample point, these splines do not model the "physics" implicit in the measurements, such as the vanishing divergence of an electric field. This report develops one class of physics-based spline with a vanishing divergence and demonstrates these splines are better interpolants of electric fields than the standard splines.

Section 1.1 introduces the standard cubic spline. Section 1.2 introduces the electric field measurements and applies the standard splines to these measurements. The differences between the splines motivate the development of the divergence-free splines. Section 1.3 sets out the divergence constraint. Section 1.4 outlines the report and sets the notation.

## 1.1 STANDARD SPLINES

Splines are interpolating functions subject to smoothness constraints. The standard *cubic spline* had its origin in the wooden and plastic splines employed by ship and aircraft designers to make smooth hulls, wings, and propellers. Figure 1 is an example of a wooden spline where both endpoints are clamped and two interpolation "nodes" bend the spline into the "S" shape.

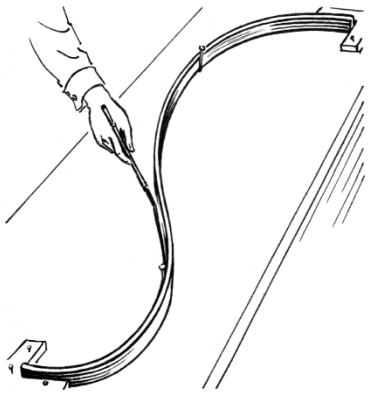

Figure 1. A wooden spline (Courtesy of Pearson Scott Foresman [6]).

Physically, this spline interpolates the nodes with minimal energy. Mathematically, a cubic spline $\psi : [a, b] \to \mathbb{R}$ is the unique function that interpolates the given data [23, Theorem 2.4.1.5]:

$$\psi(x_n) = y_n; \quad a = x_0 < x_1 \cdots x_N = b$$

with minimal "curvature"

$$C(\psi) := \int_a^b \left|\psi''(x)\right|^2 dx$$

over the class of functions on $[a, b]$ with absolutely continuous second derivative. If the interpolation points were determined by an ideal plastic spline, the cubic spline would recover the entire profile of the plastic spline using only the interpolated points.

## 1.2 STANDARD SPLINES AND THE ELECTRIC FIELD

The following figures illustrate the canonical example of this report where an electric field is estimated from sparse measurements. Figure 2 shows the measurement locations on the flight deck.

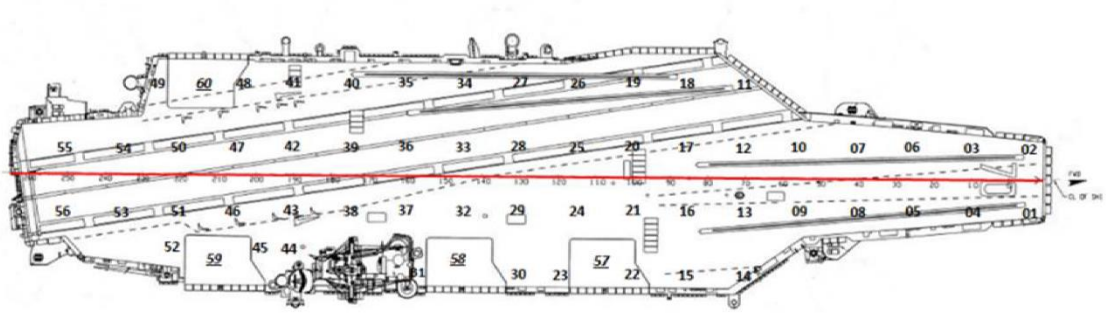


Figure 2. Electric field measurement locations on the flight deck; locations are spaced 60 feet apart in the $x$ direction. Inner rows are 36 feet from from the center line; Outer rows are 72 feet from inner rows except locations 52, 45, 44 that are 36 feet from the inner row [12].

Figure 3 plots the electric field magnitude at the specified locations on the flight deck. The bow of the ship is located at $x = 0$ feet. The stern is located at slightly past $x = 1000$ feet.

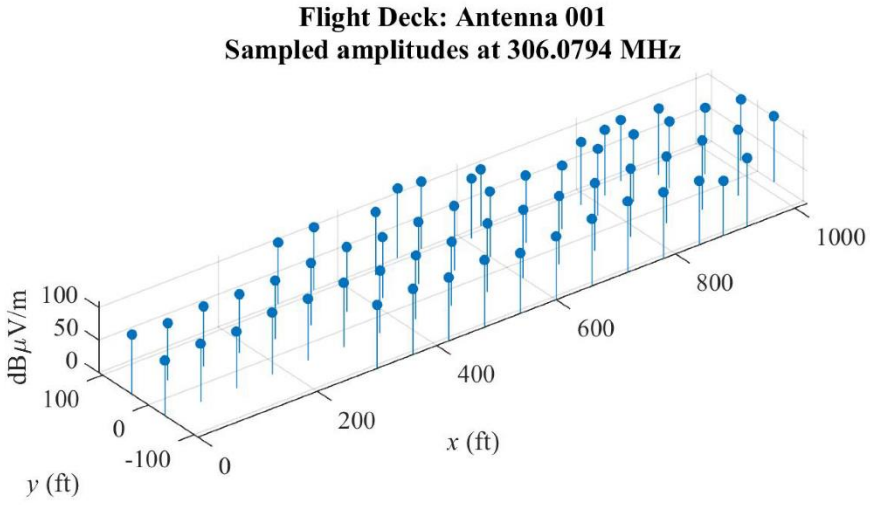


Figure 3. Electric field amplitudes at the measurement locations shown in Figure 2.

Given the scattered electric field measurements of Figure 3, the natural question asks:

*What is the electric field over the flight deck between the samples?*

Figures 4 illustrates this question by comparing 1-D interpolation of the electric field amplitudes sampled along the inner row at locations $(x_n, y_n)$ for $y_n = -36$ feet (See Figure 2). The cubic spline smoothly interpolates these amplitudes and shows the natural overshoot characteristic of these splines [23]. Making the spline "stiffer" reduces the overshooting. Stiffer splines behave more like a linear interpolant with discontinuous first derivative.

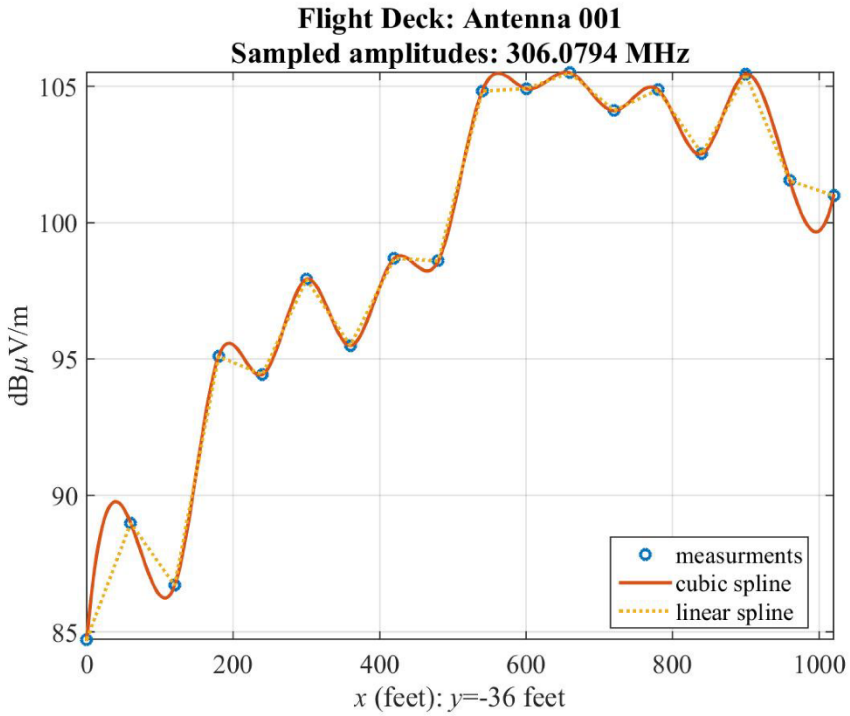


Figure 4. The linear and cubic spline interpolating measured amplitudes taken on the flight deck along the slice $y = -36$ feet.

Although both splines interpolate the measured amplitudes, the splines differ between sample points and raises the question:

*Which spline best matches the actual electric field?*

The question admits more consideration by observing the splines of Figures 4 employ only a 1-D slice of the electric field. Using all the measurements requires splines that interpolate in two dimensions. The cubic spline generalizes to interpolation over domains of two and three dimensions. Other splines that also generalize to 2-D and 3-D domains are linear interpolation [23], the natural neighbor interpolation [24] and the biharmonic spline [21]. Figures 5 and 6 apply these 2-D splines to to the flight-deck measurements.

Figures 5 is a top view of the sample points $(x_n, y_n)$ on the flight deck. Figure 6 compares three different splines interpolating the measured electric-field amplitudes at these 2-D sample points:

$$|v_n| = \psi(x_n, y_n),$$

where the absolute value sign emphasizes that the voltages are amplitude only. All the interpolants capture the gross "shape" of the electric field—more amplitude in the stern—the fields are different. Under sufficient smoothness conditions, splines converge to their source function as the sampling becomes dense [23, Theorem 2.3.3.3]. Typical splines require four or more samples per wavelength to follow a sinusoid. The measurement locations on the flight deck are approximately 20 meters apart. At 306 MHz, the wavelength is approximately $\lambda \approx 1$ meter. Therefore, additional electric-field structure must be exploited to overcome this sparse sampling.

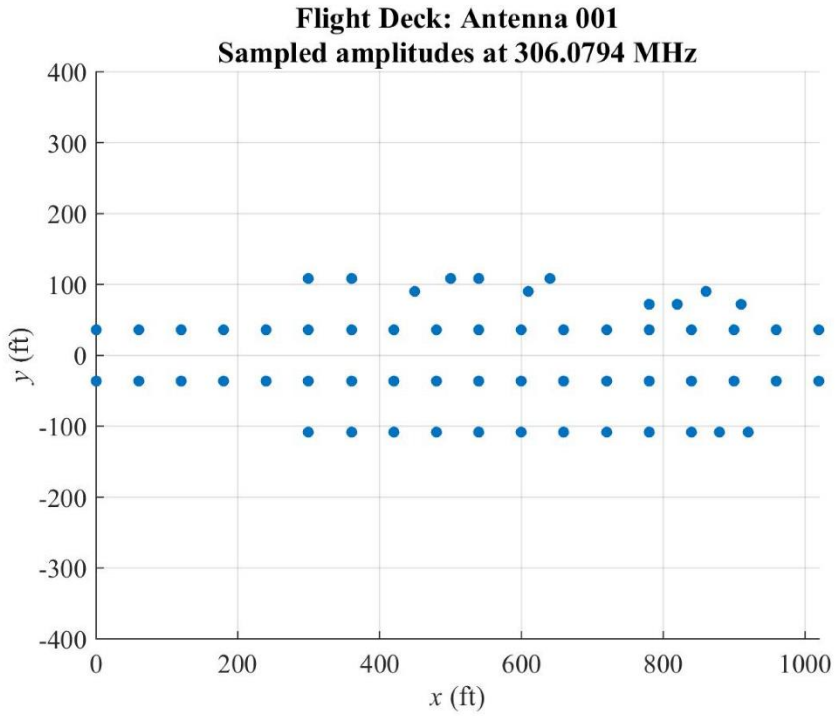


Figure 5. Measurement locations on the flight deck.

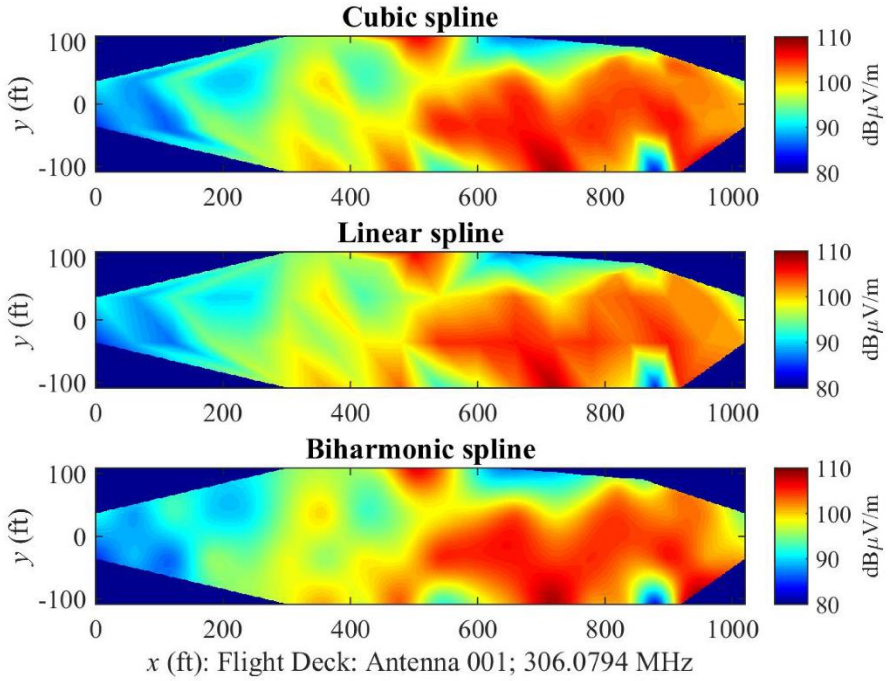


Figure 6. Splines of the electric field amplitudes using the flight-deck measurements.

### 1.3 WHY DIVERGENCE-FREE SPLINES?

Electric fields $\mathbf{E}$ in free space

$$\mathbf{E}(\mathbf{r}) = \begin{bmatrix} E_x(\mathbf{r}) \\ E_y(\mathbf{r}) \\ E_z(\mathbf{r}) \end{bmatrix}$$

have zero divergence [22, Eq. 3.4]:

$$0 = \mathrm{div}(\mathbf{E}) = \frac{\partial E_x}{\partial x} + \frac{\partial E_y}{\partial y} + \frac{\partial E_z}{\partial z}.$$

Although three cubic splines could separately interpolate each component of an electric field, the splined components are not designed to exhibit zero divergence. This report develops a class of divergence-free splines to enforce the divergence constraint and assesses the quality-of-fit on electric fields. The conclusion is that these divergence-free splines outperform the standard splines when interpolating simulated and measured electric fields.

### 1.4 OUTLINE

Section 2 sets out the formalism for a class of divergence-free splines in two and three dimensions using a Gaussian function.

Section 3 reviews electric fields and the associated plane-wave propagation in free space. These plane-wave electric fields are divergence free. The divergence-free splines produce better interpolations of these divergence-free fields than the linear, natural, or cubic splines.

Section 4 reviews the electric field generated by the Hertzian dipole in free space. This free-space model approximates the electric field generated by a Hertzian dipole over a Perfect Electrical Conductor (PEC). The divergence-free splines produce better approximations to this electrical field than the linear or cubic splines.

Section 5 applies the preceding developments to the magnitude-only electric-field measured on a flight deck. The divergence-free splines assume an electric-field model of the form:

$$\mathbf{E}(\mathbf{r}_n) = |v_n| e^{j\angle v_n} \begin{bmatrix} \cos(\phi_n)\sin(\theta_n) \\ \cos(\phi_n)\sin(\theta_n) \\ \cos(\theta_n) \end{bmatrix}$$

where only the position $\mathbf{r}_n$ and the magnitude $|v_n|$ are measured. The electric field azimuth $\{\phi_n\}$, zenith $\{\theta_n\}$, and voltage phase $\{\angle v_n\}$ are free parameters in the model. If a divergence-free spline $\vec{\psi}(\mathbf{r})$ interpolates this synthetic electric field

$$\vec{\psi}(\mathbf{r}_n) = \mathbf{E}(\mathbf{r}_n),$$

the magnitude is interpolated at each sample point:

$$\|\vec{\psi}(\mathbf{r}_n)\| = \|\mathbf{E}(\mathbf{r}_n)\| = |v_n|$$

while free parameters are optimized to meet other modeling constraints. In this report, the electric field model is optimized to minimize the distance between the divergence-free spline and the cubic spline. That is, the resulting spline represents a divergence-free electric field that is also closest to a standard spline.

Section 6 details how a UAV, carrying a three-axis antenna to measure the electric field, could rapidly sample a relatively large electric field for interpolation by divergence-free splines. In particular, the electric field over a flight deck could be densely sampled in a volume over the deck to caputre the 3-D view of the electric field rather than the horizontal slice.

### 1.5 NOTATION

The real numbers are denoted by $\mathbb{R}$. The real vector space of dimension $d$ is denoted by $\mathbb{R}^d$. The complex numbers are denoted by $\mathbb{C}$. The complex vector space of dimension $d$ is denoted by $\mathbb{C}^d$. A spatial vector $\mathbf{r} \in \mathbb{R}^3$ is typically written

$$\mathbf{r} = \begin{bmatrix} x \\ y \\ z \end{bmatrix}.$$

The transpose of a vector is

$$\mathbf{r}^{\mathsf{T}} = \begin{bmatrix} x & y & z \end{bmatrix}.$$

The vector norm is

$$\|\mathbf{r}\| = \sqrt{\mathbf{r}^{\mathsf{T}}\mathbf{r}} = \sqrt{x^2 + y^2 + z^2}.$$

An electric field vector at a location $\mathbf{r} \in \mathbb{R}^3$ has complex-valued components denoted as

$$\mathbf{E}(\mathbf{r}) = \begin{bmatrix} E_x(\mathbf{r}) \\ E_y(\mathbf{r}) \\ E_z(\mathbf{r}) \end{bmatrix}.$$

The "nabla" operator is [7]

$$\nabla = \begin{bmatrix} \partial/\partial x \\ \partial/\partial y \\ \partial/\partial z \end{bmatrix}$$

and employed as a vector so that

$$\mathrm{div}(\mathbf{E}) = \nabla^{\mathsf{T}}\mathbf{E} = \frac{\partial E_x}{\partial x} + \frac{\partial E_y}{\partial y} + \frac{\partial E_z}{\partial z}.$$

The inner product of the nabla with itself is the Laplacian:

$$\Delta = \nabla^{\mathsf{T}}\nabla = \frac{\partial^2}{\partial x^2} + \frac{\partial^2}{\partial y^2} + \frac{\partial^2}{\partial z^2}.$$

The outer product of the nabla with itself is the second-derivative matrix

$$\nabla\nabla^{\mathsf{T}} = \begin{bmatrix} \frac{\partial^2}{\partial x^2} & \frac{\partial^2}{\partial x \partial y} & \frac{\partial^2}{\partial x \partial z} \\ \frac{\partial^2}{\partial y \partial x} & \frac{\partial^2}{\partial y^2} & \frac{\partial^2}{\partial y \partial z} \\ \frac{\partial^2}{\partial z \partial x} & \frac{\partial^2}{\partial z \partial y} & \frac{\partial^2}{\partial z^2} \end{bmatrix}$$

that acts on a scalar function $\psi$ as

$$\nabla\nabla^{\mathsf{T}}\psi = \begin{bmatrix} \frac{\partial^2 \psi}{\partial x^2} & \frac{\partial^2 \psi}{\partial x \partial y} & \frac{\partial^2 \psi}{\partial x \partial z} \\ \frac{\partial^2 \psi}{\partial y \partial x} & \frac{\partial^2 \psi}{\partial y^2} & \frac{\partial^2 \psi}{\partial y \partial z} \\ \frac{\partial^2 \psi}{\partial z \partial x} & \frac{\partial^2 \psi}{\partial z \partial y} & \frac{\partial^2 \psi}{\partial z^2} \end{bmatrix}.$$

The Laplacian multiplies the $3 \times 3$ identity matrix $I_3$ as

$$\Delta \cdot I_3 = \Delta \begin{bmatrix} 1 & 0 & 0 \\ 0 & 1 & 0 \\ 0 & 0 & 1 \end{bmatrix}$$

and acts on a scalar-valued function $\psi$ as

$$\Delta \cdot I_3 \psi = \Delta \begin{bmatrix} \Delta\psi & 0 & 0 \\ 0 & \Delta\psi & 0 \\ 0 & 0 & \Delta\psi \end{bmatrix}.$$

# 2. DIVERGENCE-FREE SPLINES

The divergence-free interpolation problem seeks a vector field $\vec{\psi}$ that interpolates vector-valued measurements $\mathbf{v}_n$ at spatial locations $\mathbf{r}_n$:

$$\mathbf{v}_n = \vec{\psi}(\mathbf{r}_n)$$

with vanishing divergence:

$$0 = \nabla^{\mathsf{T}} \vec{\psi}(\mathbf{r})$$

for all $\mathbf{r} \in \mathbb{R}^d$, where $d$ denotes the spatial dimension ($d = 2, 3$).

In 1982, Grace Wahba produced one of the first papers on splines that obeyed physical laws [25]. This paper estimated *divergence-free* and *curl-free* splines on the sphere from discrete and noisy measurements. By 1992, the mathematical community had generalized divergence-free splines to divergence-free vector wavelets. By 1994, "wavelet electromagnetics" reached book form [13]. Multiple approaches are summarized by Lemarie-Rieusset's 1992 paper [17]. The "top-down" approach constructs a wavelet basis of $L^2(\mathbb{R}^d, \mathbb{R})$ with projections $P_j$ and a wavelet basis of $L^2(\mathbb{R}^d, \mathbb{R}^d)$ with projections $\vec{P}_j$ that commute with the divergence operator [11]:

$$\nabla^{\mathsf{T}} \vec{P}_j \vec{\psi} = P_j \nabla^{\mathsf{T}} \vec{\psi}.$$

The "bottom-up" approach converts a wavelet basis $\{\psi_{j,k}\}$ into a divergence-free basis. This report uses a bottom-up approach to develop a class of divergence-free splines when the wavelets are generated by Gaussian functions.

### 2.1 GAUSSIAN SPLINES

The 2011 paper by McNally uses Gaussian functions to parameterize a class of divergence-free splines. [18]. Let $\psi$ denote the Gaussian function of the form

$$\psi(\mathbf{r}) := \exp(-\beta \mathbf{r}^{\mathsf{T}} \mathbf{r}); \quad \beta > 0. \tag{1}$$

Define the matrix-valued function

$$\Psi = \left\{ \nabla \nabla^{\mathsf{T}} - \Delta I_d \right\} \psi, \tag{2}$$

where $I_d$ denotes the $d \times d$ identity matrix. This function has zero divergence because

$$\begin{aligned} \nabla^{\mathsf{T}} \left\{ \nabla \nabla^{\mathsf{T}} - \Delta I_d \right\} &= \nabla^{\mathsf{T}} \nabla \nabla^{\mathsf{T}} - \nabla^{\mathsf{T}} \Delta I_d \\ &= \Delta \nabla^{\mathsf{T}} - \Delta \nabla^{\mathsf{T}} \\ &= 0. \end{aligned}$$

Sections 2.2 and 2.3 detail the interpolation conditions for $d = 2$ and 3, respectively.

### 2.2 GAUSSIAN SPLINES IN TWO DIMENSIONS

The Gaussian spline matrix $\Psi$ of Equation 2 in two dimensions is

$$\Psi(\beta;\mathbf{r}) := 2\beta\psi(x,y)\begin{bmatrix}1-2\beta y^2 & 2\beta xy\\ 2\beta xy & 1-2\beta x^2\end{bmatrix}, \tag{3}$$

where $\psi$ is the Gaussian function of Equation 1. The Gaussian spline

$$\vec{\psi}(\mathbf{r}) = \begin{bmatrix}\psi_1(\mathbf{r})\\ \psi_2(\mathbf{r})\end{bmatrix} := \sum_{n=1}^{N}\Psi(\beta_n;\mathbf{r}-\mathbf{r}_n)\mathbf{w}_n$$

interpolates electric field measurements $\{\mathbf{r}_n,\mathbf{v}_n\}$ as

$$\mathbf{v}_n = \begin{bmatrix}\psi_1(\mathbf{r}_n)\\ \psi_2(\mathbf{r}_n)\end{bmatrix};\quad (n=1,\ldots,N)$$

if and only if the Vandermode matrix with the $2\times 2$ blocks is invertible:

$$\begin{bmatrix}\mathbf{v}_1\\ \mathbf{v}_2\\ \vdots\\ \mathbf{v}_N\end{bmatrix} = \begin{bmatrix}2\beta_1 I_2 & \Psi(\beta_2;\mathbf{r}_1-\mathbf{r}_2) & \cdots & \Psi(\beta_N;\mathbf{r}_1-\mathbf{r}_N)\\ \Psi(\beta_1;\mathbf{r}_2-\mathbf{r}_1) & 2\beta_2 I_2 & \cdots & \Psi(\beta_N;\mathbf{r}_2-\mathbf{r}_N)\\ \vdots & \vdots & \ddots & \vdots\\ \Psi(\beta_1;\mathbf{r}_N-\mathbf{r}_1) & \Psi(\beta_2;\mathbf{r}_N-\mathbf{r}_2) & \cdots & 2\beta_N I_2\end{bmatrix}\begin{bmatrix}\mathbf{w}_1\\ \mathbf{w}_2\\ \vdots\\ \mathbf{w}_N\end{bmatrix}. \tag{4}$$

Figures 7 and 8 show the field and magnitude of the first column

$$\Psi(:,1) = \begin{bmatrix}\psi_{11}\\ \psi_{21}\end{bmatrix}.$$

Likewise, Figures 9 and 10 show the field and magnitude of the second column

$$\Psi(:,2) = \begin{bmatrix}\psi_{12}\\ \psi_{22}\end{bmatrix}.$$

McNally [18] insightfully observes that the first column of $\Psi$ "resembles a dipole field in the $x$ direction" and that the second column of $\Psi$ resembles "a dipole field in the $y$ direction." This interpolation method is divergence free because "the field is built entirely from shifted and normalized versions of the dipole components." Using these Gaussian splines requires an adroit selection of the $\beta_n$'s. Relatively large values of the $\beta_n$'s produce divergence-free fields consisting of Gaussian "thumbtacks" as illustrated by Figures 8 and 10. More substantial problems arise when only the magnitude of the electric field is measured.

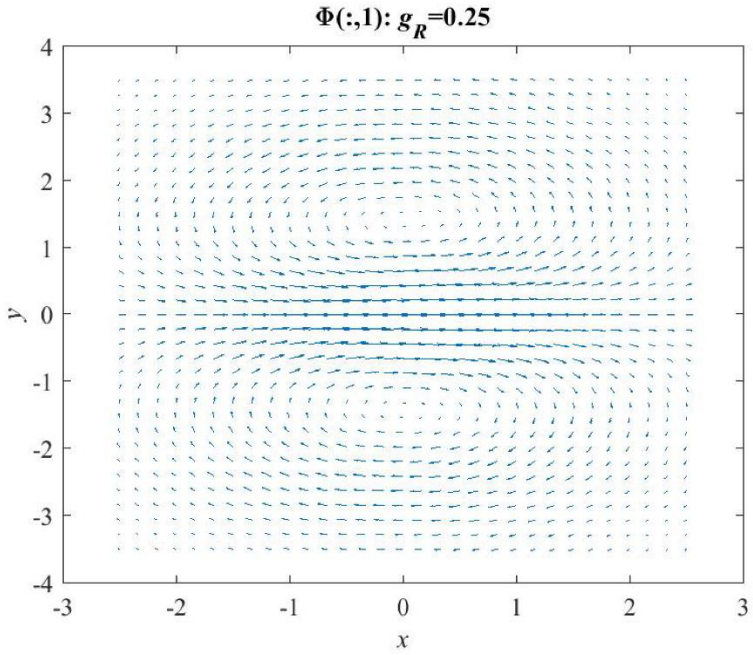


Figure 7. Vector field of the first column of $\Psi(\beta, \mathbf{r})$.

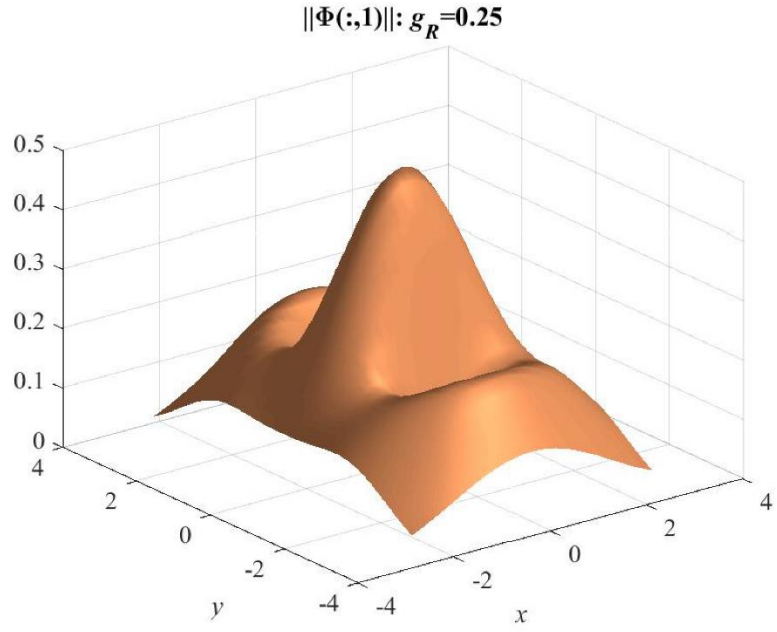


Figure 8. Magnitude of the first column of $\Psi(\beta, \mathbf{r})$.

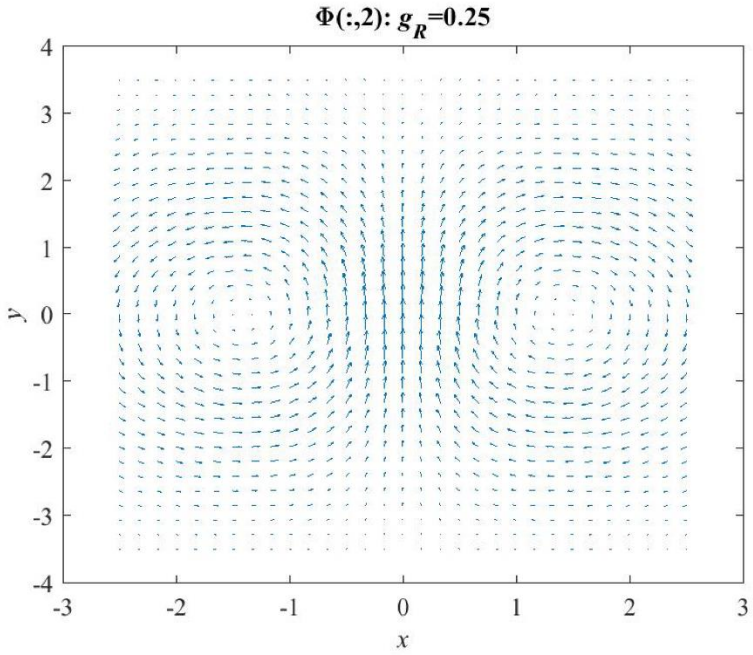


Figure 9. Vector field of the second column of $\Psi(\beta, \mathbf{r})$.

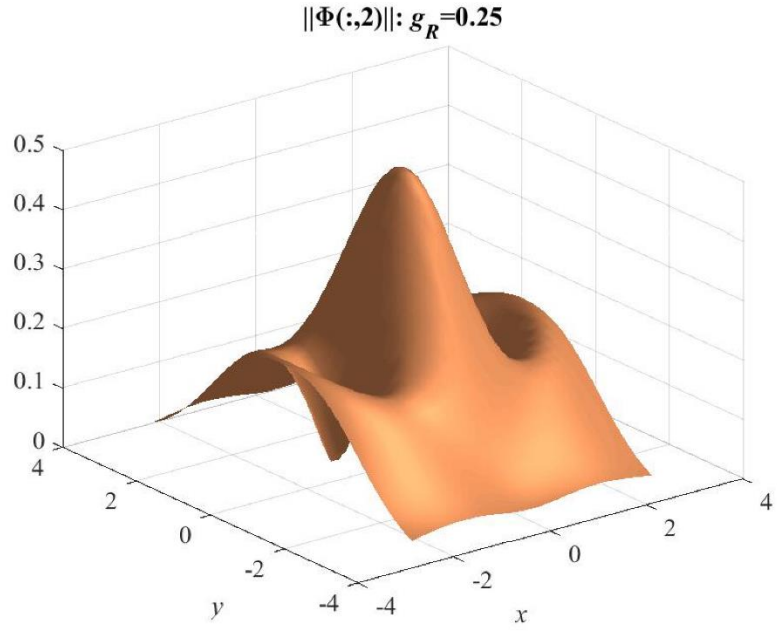


Figure 10. Magnitude of the second column of $\Psi(\beta, \mathbf{r})$.

### 2.3 GAUSSIAN SPLINES IN THREE DIMENSIONS

The Gaussian spline matrix $\Psi$ of Equation 2 is three dimensions is

$$\Psi(\beta;\mathbf{r}) = 4\beta\psi(x,y,z)\begin{bmatrix} 1-\beta(y^2+z^2) & \beta xy & \beta xz \\ \beta xy & 1-\beta(x^2+z^2) & \beta yz \\ \beta xz & \beta yz & 1-\beta(x^2+y^2) \end{bmatrix},$$

where $\psi$ is the Gaussian function of Equation 1. The Gaussian spline

$$\vec{\psi}(\mathbf{r}) = \begin{bmatrix} \psi_1(\mathbf{r}) \\ \psi_2(\mathbf{r}) \\ \psi_3(\mathbf{r}) \end{bmatrix} := \sum_{n=1}^{N} \Psi(\beta_n;\mathbf{r}-\mathbf{r}_n)\mathbf{w}_n$$

interpolates the electric field as

$$\mathbf{v}_n = \begin{bmatrix} \psi_1(\mathbf{r}_n) \\ \psi_2(\mathbf{r}_n) \\ \psi_3(\mathbf{r}_n) \end{bmatrix}; \quad (n=1,\ldots,N)$$

if and only if the Vandermode matrix with the $3\times 3$ blocks is invertible:

$$\begin{bmatrix} \mathbf{v}_1 \\ \mathbf{v}_2 \\ \vdots \\ \mathbf{v}_N \end{bmatrix} = \begin{bmatrix} 4\beta_1 I_3 & \Psi(\beta_2;\mathbf{r}_1-\mathbf{r}_2) & \cdots & \Psi(\beta_N;\mathbf{r}_1-\mathbf{r}_N) \\ \Psi(\beta_1;\mathbf{r}_2-\mathbf{r}_1) & 4\beta_2 I_3 & \cdots & \Psi(\beta_N;\mathbf{r}_2-\mathbf{r}_N) \\ \vdots & \vdots & \ddots & \vdots \\ \Psi(\beta_1;\mathbf{r}_N-\mathbf{r}_1) & \Psi(\beta_2;\mathbf{r}_N-\mathbf{r}_2) & \cdots & 4\beta_N I_3 \end{bmatrix} \begin{bmatrix} \mathbf{w}_1 \\ \mathbf{w}_2 \\ \vdots \\ \mathbf{w}_N \end{bmatrix}. \tag{5}$$

Figures 11, 12, 13 plot the vector fields generated by the three colmns of $\Psi$. The plots show that each column $\Psi(:,1)$, $\Psi(:,2)$, $\Psi(:,3)$ is a dipole field pattern along the $x$, $y$, and $z$ axis, respectively.

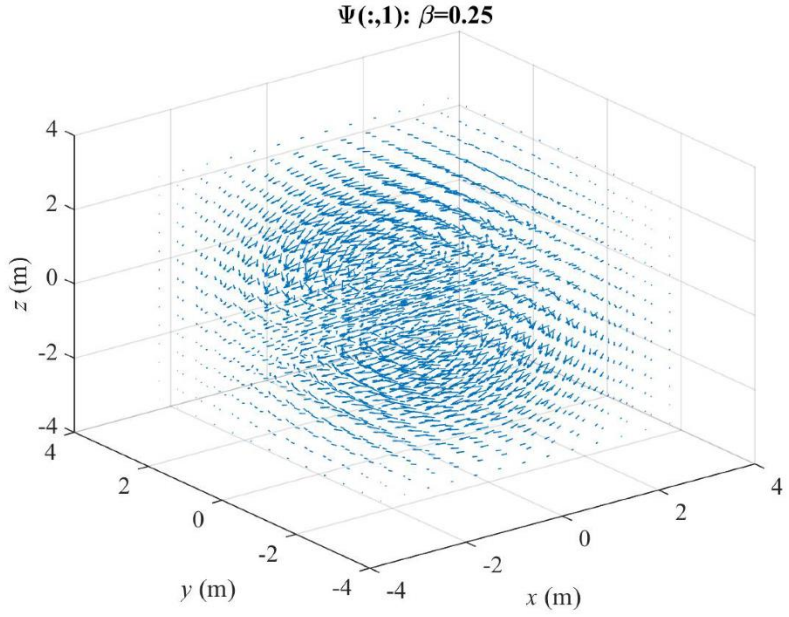


Figure 11. 3-D vector field of the first column of $\Psi(\beta,\mathbf{r})$.

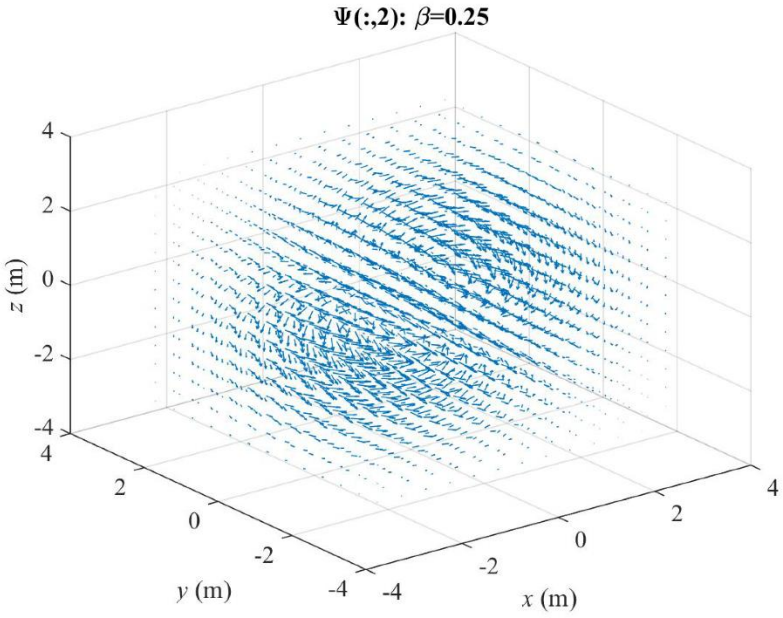


Figure 12. 3-D vector field of the second column of $\Psi(\beta, \mathbf{r})$.

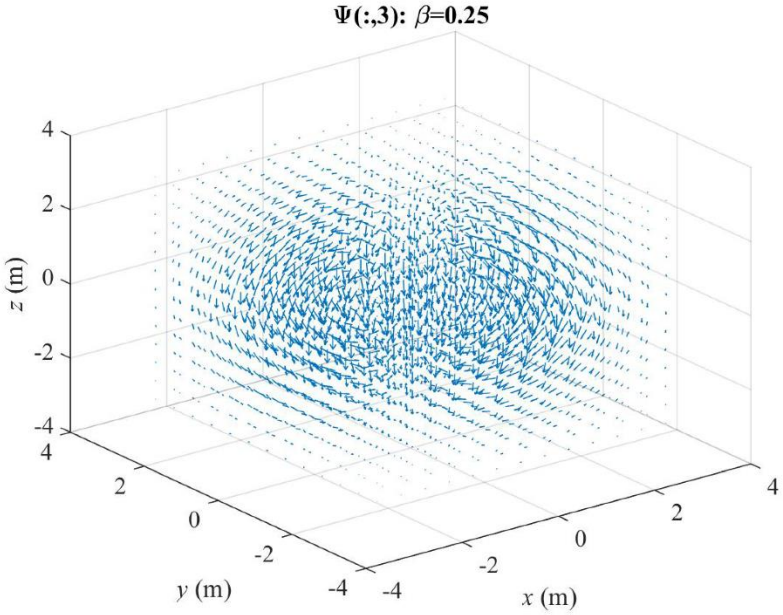


Figure 13. 3-D vector field of the third column of $\Psi(\beta, \mathbf{r})$.

# 3. SPLINES OF PLANE WAVES

This section splines the electric field produced by plane waves propagating in two- and three-dimensional free space. In both cases, the divergence-free Gaussian splines are better interpolants of the plane-wave electric fields than the cubic, natural, and linear splines. Section 3.1 sets out the plane-wave models. Sections 3.2 and 3.3 compare the splines on 2-D and 3-D plane waves, respectively.

## 3.1 ELECTRIC-FIELD PLANE WAVES IN FREE SPACE

This section reviews electric field theory to set up analytic models of selected electric fields consisting of a sum of plane waves. The analytic models are the baseline to compare the divergence-free splines against the standard splines. Maxwell's Equations in free space take the form [5]:

$$\begin{aligned} \nabla \times \mathbf{E} &= -j\omega\mu_0\mathbf{H} \\ \nabla \times \mathbf{H} &= (\sigma + j\omega\epsilon_0)\mathbf{E} \\ \nabla^{\mathsf{T}}\mathbf{E} &= 0 \\ \nabla^{\mathsf{T}}\mathbf{H} &= 0 \end{aligned}$$

where the free-space permeability is $\mu_0 = 4\pi \cdot 10^{-7}$ H/m, the free-space permittivity is $\epsilon_0 = 8.85 \cdot 10^{-12}$ F/m, and the angular frequency $\omega$ is in rad/sec. Gauss' Law is the third equation where the vanishing divergence has the physical meaning that the net electric flux though any closed surface that surrounds no charge is zero.

**Wave Equation:** The electric field in free space satisfies the wave equation [22, Eq. 3.5]:

$$\nabla^2\mathbf{E} + \omega^2\mu_0\epsilon_0\mathbf{E} = \mathbf{0}.$$

The wavenumber appears in the wave equation as [22, Eq. 3.7]

$$k^2 = \omega^2\mu_0\epsilon_0$$

because [22, Eq. 3.9]

$$k := \frac{2\pi}{\lambda} = \frac{\omega}{c_0} \quad \text{[rad/m]}$$

and the speed of propagation $c_0$ is

$$c_0 = \frac{1}{\sqrt{\mu_0\epsilon_0}} \quad \text{[m/sec]}.$$

**Wave Equation Solutions:** *Plane-wave* solutions of the wave equation depend on only one spatial direction and have the general form [5, page 218]:

$$\mathbf{E}(\mathbf{r}) := u(\mathbf{r})\mathbf{e}_0 \quad [\mathrm{V/m}],$$

where $\mathbf{e}_0 \in \mathbb{C}^3$ and $u(\mathbf{r})$ satisfies the scalar wave equation. Time-harmonic plane waves have the form

$$\mathbf{E}(\mathbf{r}) := \exp(-j\mathbf{k}^{\mathsf{T}}\mathbf{r})\mathbf{e}_0; \quad k = \|\mathbf{k}\|,$$

where $\mathbf{k}$ is called the *wave vector*. This electric field is divergence-free provided the electric field vector $\mathbf{e}_0$ is orthogonal to the wave vector:

$$0 = \mathbf{k}^{\mathsf{T}}\mathbf{e}_0 \iff \nabla^{\mathsf{T}}\mathbf{E} = 0.$$

**Parametrization:** This report parameterizes plane wave electric fields as

$$\mathbf{E}(\mathbf{r}) = \exp(-j\mathbf{k}^{\mathsf{T}}\mathbf{r})\mathbf{e}_0; \quad \mathbf{k} = k\begin{bmatrix}\cos(\phi)\sin(\theta)\\ \sin(\phi)\sin(\theta)\\ \cos(\theta)\end{bmatrix}; \quad k = \frac{2\pi}{\lambda}, \tag{6}$$

using the azimuth angle $\phi$ and zenith angle $\theta$ as shown in Figure 14.

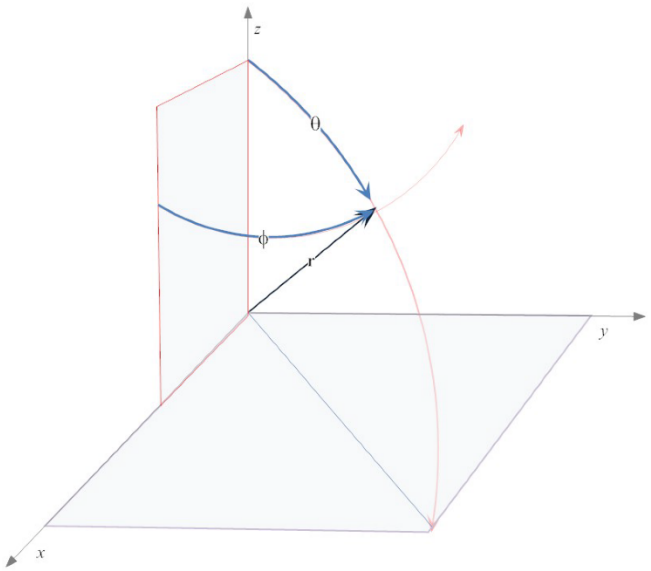


Figure 14. Spherical coordinates.

**Power Flow:** The Poynting vector determines the direction of power flow [22, Eq. 2.31]

$$\mathbf{S} = \mathbf{E} \times \mathbf{H}^* \quad [\mathrm{W/m^2}],$$

where $\mathbf{H}$ is the magnetic field. The magnetic field is the curl of the electric field [22, Eq. 3.1]:

$$\frac{1}{-j\omega\mu_0}\nabla \times \mathbf{E} = \mathbf{H} \quad [\mathrm{A/m}].$$

The curl of the plane-wave electric field determines the magnetic field as

$$\mathbf{H} = \exp(-j\mathbf{k}^{\mathsf{T}}\mathbf{r})\mathbf{h}_0; \quad \mathbf{h}_0 := \frac{1}{\omega\mu_0}\mathbf{k} \times \mathbf{e}_0.$$

Consequently, this magnetic field is also orthogonal to $\mathbf{k}$ and divergence-free:

$$0 = \mathbf{k}^{\mathsf{T}} \times \mathbf{h}_0 \iff \nabla^{\mathsf{T}}\mathbf{H} = 0.$$

Therefore, the Poynting vector is constant [22, Eq. 2.31]

$$\mathbf{S} = \mathbf{e}_0 \times \mathbf{h}_0 \quad [\mathrm{W \cdot m^2}]$$

and points along the wave vector $\mathbf{k}$ because $\mathbf{e}_0$ and $\mathbf{h}_0$ are both orthogonal to $\mathbf{k}$.

**Example 1 (Plane Wave Along the $x$ Axis)** *If the wave vector* $\mathbf{k}$ *points along the* $x$*-axis*

$$\mathbf{k} = k \begin{bmatrix} 1 \\ 0 \\ 0 \end{bmatrix}; \quad k = \frac{2\pi}{\lambda} \quad [\text{rad/m}]$$

*and the electric field direction points along the* $y$*-axis*

$$\mathbf{e}_0 = \begin{bmatrix} 0 \\ 1 \\ 0 \end{bmatrix} \quad [\text{V/m}],$$

*the electric field is*

$$\mathbf{E}(\phi; \mathbf{r}) = \exp(-j\mathbf{k}^{\mathsf{T}}\mathbf{r})\mathbf{e}_0 = e^{-jkx} \begin{bmatrix} 0 \\ 1 \\ 0 \end{bmatrix} \quad [\text{V/m}].$$

*The magnetic field is*

$$\mathbf{H} = \frac{1}{-j\omega\mu_0}\nabla \times \mathbf{E} = \frac{e^{-jkx}}{c_0\mu_0} \begin{bmatrix} 0 \\ 0 \\ 1 \end{bmatrix} \quad [\text{A/m}]$$

*so that the Poynting vector* $\mathbf{S}$ *has the same direction as the wave vector:*

$$\mathbf{S} = \mathbf{E} \times \mathbf{H}^* = \frac{1}{c_0\mu_0} \begin{bmatrix} 0 \\ 1 \\ 0 \end{bmatrix} \times \begin{bmatrix} 0 \\ 0 \\ 1 \end{bmatrix} = \frac{1}{c_0\mu_0} \begin{bmatrix} 1 \\ 0 \\ 0 \end{bmatrix}.$$

### 3.2 SPLINES OF 2-D PLANE WAVES

This section compares several splines against the 2-D Gaussian splines on plane-wave electric fields. For simplicity, these fields are constrained to have vanishing $z$ component. The examples show that the 2-D Gaussian splines recover the electric field using fewer samples than the standard splines.

**Example 2 (Horizontal Plane Wave)** *If the electric field has no $z$ component, the wave vector $\mathbf{k}_\phi$ is determined by the azimuth angle $\phi$ as*

$$\mathbf{k}_\phi = k \begin{bmatrix} \cos(\phi) \\ \sin(\phi) \\ 0 \end{bmatrix}; \quad k = \frac{2\pi}{\lambda} \quad [\text{rad/m}].$$

*For the plane-wave electric field to be divergence-free, $\mathbf{e}_\phi$ must be orthogonal to wave vector $\mathbf{k}_\phi$. Selecting*

$$\mathbf{e}_\phi = \begin{bmatrix} \sin(\phi) \\ -\cos(\phi) \\ 0 \end{bmatrix} \quad [\text{V/m}]$$

*determines the electric field as*

$$\mathbf{E}(\phi; \mathbf{r}) = \cos(\mathbf{k}_\phi^\top \mathbf{r})\mathbf{e}_\phi = \begin{bmatrix} E_1(\phi; \mathbf{r}) \\ E_2(\phi; \mathbf{r}) \\ 0 \end{bmatrix} \quad [\text{V/m}].$$

*For comparison with the shipboard measurements, the center frequency is set to $f_C = 300$ MHz or, equivalently, the wavelength is $\lambda = 1$ meter. Figure 15 plots the first two components of the electric field over the rectangle $0 \le x \le 10$ and $-1 \le y \le 1$ meters. Figure 16 shows the randomly scattered sample points $\{\mathbf{r}_n\}$ with an approximate sampling density of*

$$\rho = \frac{79}{2 \times 10} \approx 4 \quad [\text{samples/m}^2].$$

*Figure 17 reports the 2-D Gaussian spline based on these scattered points. Both components of the electric field are recovered with reasonable accuracy. Some distortion is visible where the randomly scattered samples are less dense. Figures 18 and 19 show that the linear or the natural splines do not recover the electric field at this sampling density.*

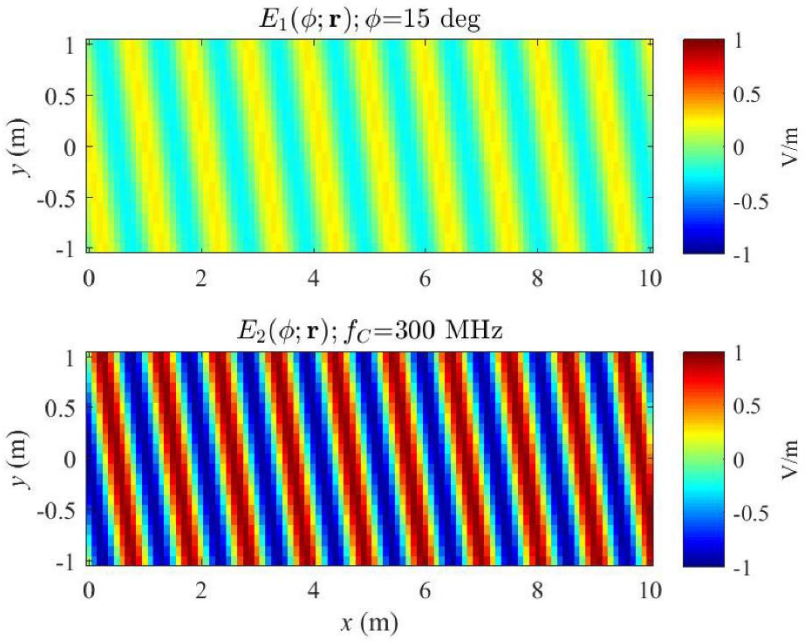


Figure 15. 2-D electric field propagating at $15^\circ$ azimuth at 300 MHz.

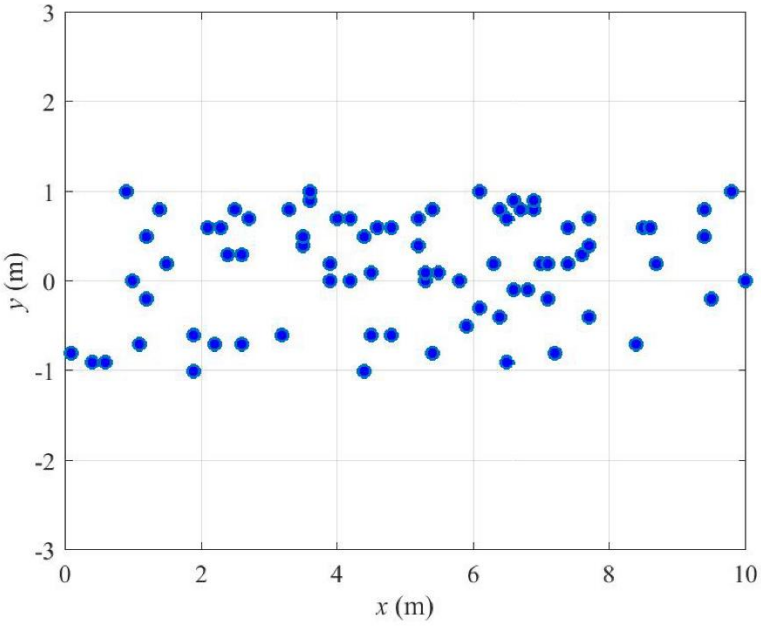


Figure 16. Randomly scattered sample points of the electric field.

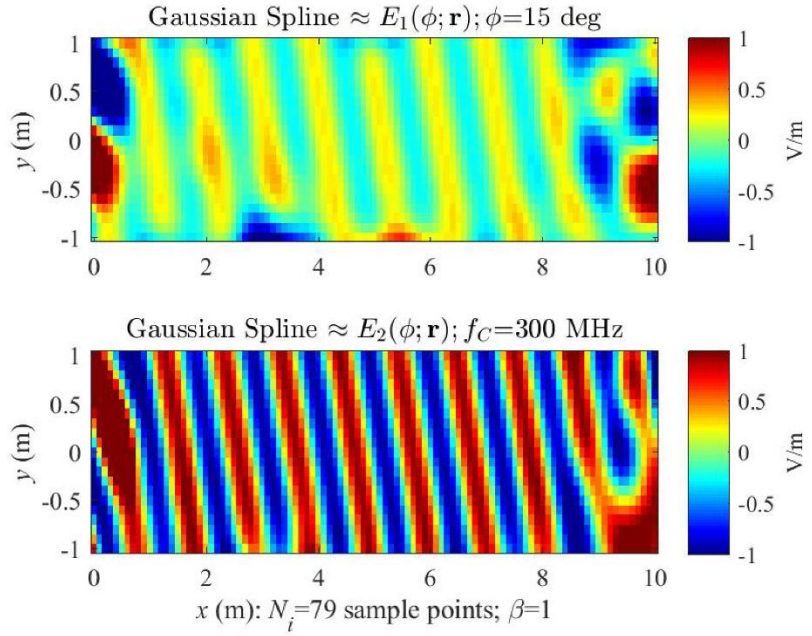


Figure 17. 2-D Gaussian spline interpolating the random samples of the electric field.

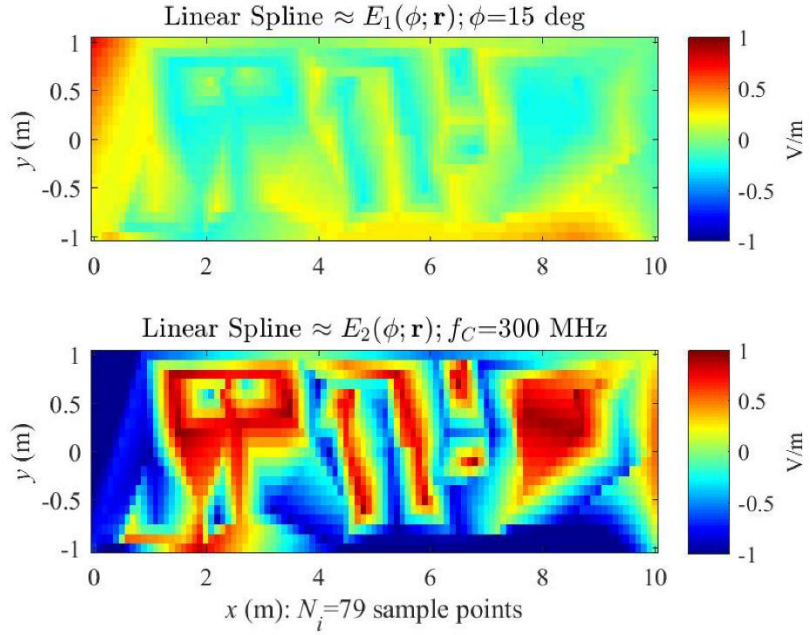


Figure 18. 2-D linear spline separately interpolating each electric field component using the random samples of the electric field.

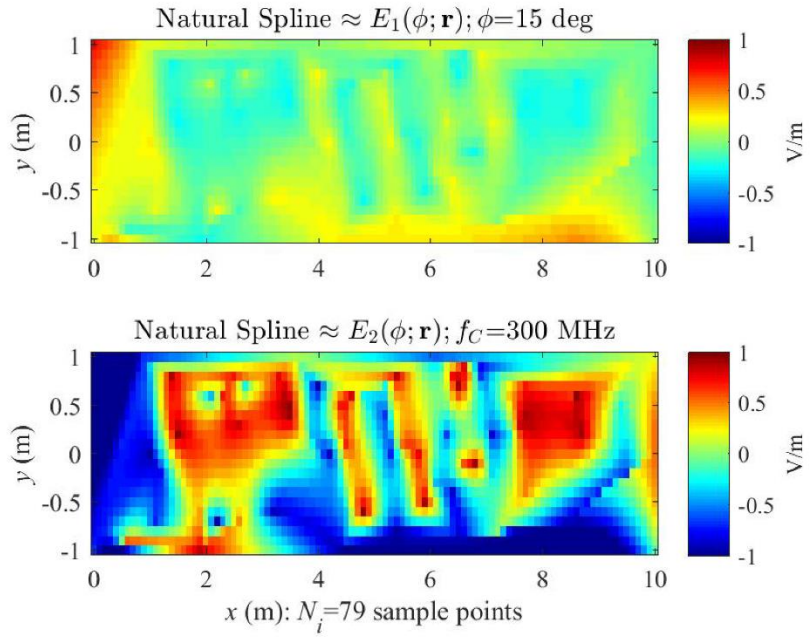


Figure 19. 2-D natural spline separately interpolating each electric field component using the random samples of the electric field.

Example 2 employs 2-D splines interpolating the electric field components $\{E_1(\mathbf{r}_n)\}$ and $\{E_2(\mathbf{r}_n)\}$ at the randomly scattered sample points $\{\mathbf{r}_n\}$. For concreteness, the following Matlab code fragment makes explicit the interpolation of the electric field using the scattered interpolating points:

```
% Linear spline of the scattered electric field
e1Spline = scatteredInterpolant( xI(:), yI(:), V(1,:)', 'linear' );
e1Linear = e1Spline(X,Y);
e2Spline = scatteredInterpolant( xI(:), yI(:), V(2,:)', 'linear');
e2Linear = e2Spline(X,Y);

% Natural spline
e1Spline = scatteredInterpolant( xI(:), yI(:), V(1,:)', 'natural' );
e1Nat    = e1Spline(X,Y);
e2Spline = scatteredInterpolant( xI(:), yI(:), V(2,:)', 'natural');
e2Nat    = e2Spline(X,Y);
```

Higher-order splines are more conveniently applied when the sample points lie on a grid. The next example compares the 2-D Gaussian spline to the standard splines on a rectangular grid.

**Example 3 (Rectangular Sampling)** *Assume the electric field is the same as Example 1 and plotted in Figure 15:*

$$\begin{aligned}
\mathbf{E}(\phi;\mathbf{r}) &= \cos(\mathbf{k}_\phi^{\mathsf{T}}\mathbf{r})\mathbf{e}_\phi = \begin{bmatrix} E_1(\phi;\mathbf{r}) \\ E_2(\phi;\mathbf{r}) \\ 0 \end{bmatrix} \quad [\mathrm{V/m}] \\
\mathbf{k}_\phi &= k \begin{bmatrix} \cos(\phi) \\ \sin(\phi) \\ 0 \end{bmatrix}; \quad k = \frac{2\pi}{\lambda} \quad [\mathrm{radians/m}] \\
\mathbf{e}_\phi &= \begin{bmatrix} \sin(\phi) \\ -\cos(\phi) \\ 0 \end{bmatrix} \quad [\mathrm{V/m}].
\end{aligned}$$

*Figure 20 shows the sample points $\{\mathbf{r}_n\}$ in a rectangular grid. Figure 21 reports the 2-D Gaussian spline using samples from this rectangular grid. Both components of the electric field are recovered with reasonable accuracy. Figure 22 and 23 report that both the linear and cubic spline show a curious distortion of the electric field.*

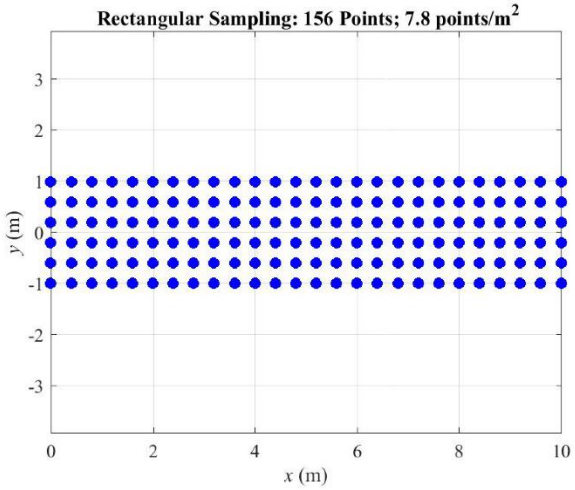


Figure 20. Rectangular sample points.

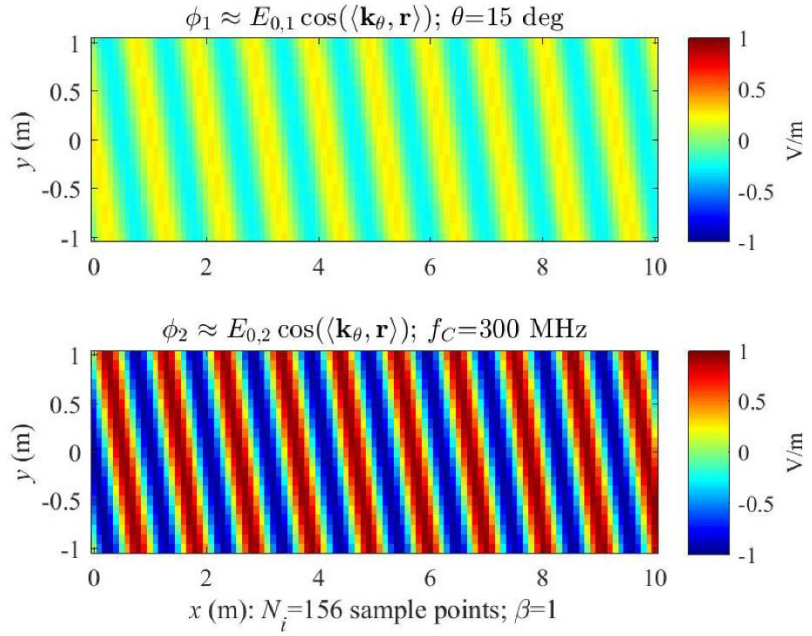


Figure 21. 2-D Gaussian spline interpolating the electric field sampled on a rectangular grid.

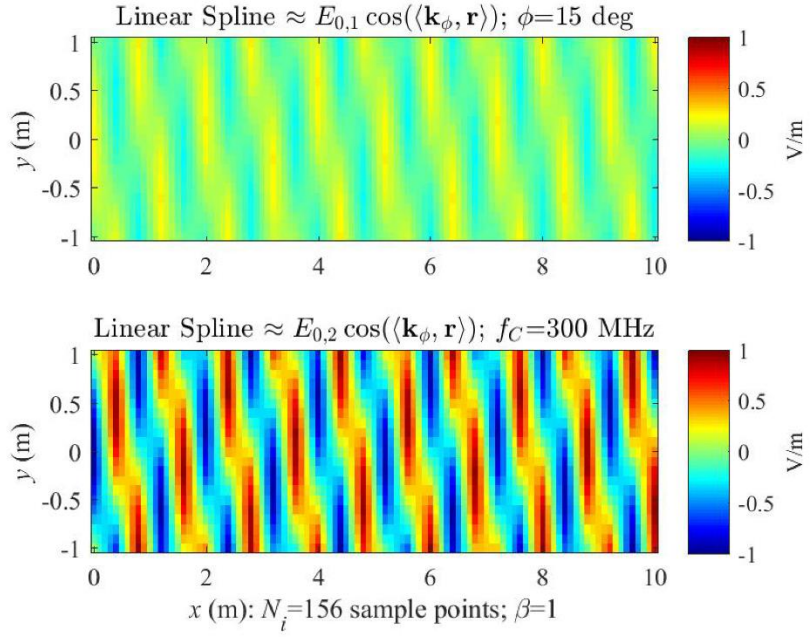


Figure 22. 2-D linear spline interpolating the electric field sampled on a rectangular grid exhibiting a periodic distortion.

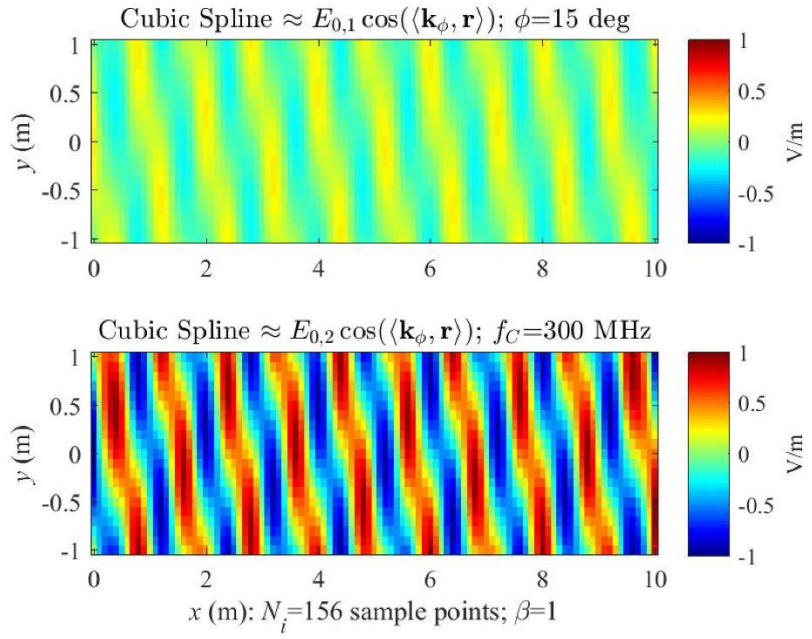


Figure 23. 2-D cubic spline interpolating the electric field sampled on a rectangular grid exhibiting a periodic distortion.

Example 3 employs 2-D splines interpolating the electric field components $\{E_1(\mathbf{r}_n)\}$ and $\{E_2(\mathbf{r}_n)\}$ on the rectangular grid of sample points $\{\mathbf{r}_n\}$ in Figure 20. For concreteness, the following Matlab code fragment makes explicit the linear and cubic splines of the electric field using these grid points are separately applied to each component of the electric field.

```
% 3. Cubic spline
e1CubicSpline = interp2( xI, yI, e1I, X, Y, 'cubic' );
e2CubicSpline = interp2( xI, yI, e2I, X, Y, 'cubic' );

% 4. Linear spline
e1LinearSpline = interp2( xI, yI, e1I, X, Y, 'linear' );
e2LinearSpline = interp2( xI, yI, e2I, X, Y, 'linear' );
```

The final example of this section shows that mixing multiple plane waves produces interesting electric fields to further assess the 2-D Gaussian spline.

**Example 4 (Two Horizontal Plane Waves)** *Assume the electric field is the sum two electric fields propagating in the $x$-$y$ plane*

$$\mathbf{E}(\vec{\phi},\mathbf{v};\mathbf{r}) = \Re\left[v_1\mathbf{u}(\phi_1;\mathbf{r}) + v_2\mathbf{u}(\phi_2;\mathbf{r})\right] =: \begin{bmatrix} E_1(\vec{\phi},\mathbf{v};\mathbf{r}) \\ E_2(\vec{\phi},\mathbf{v};\mathbf{r}) \\ 0 \end{bmatrix}$$

*parameterized by the voltages $v_{1,2} = 1,\ 1/2$ and the plane-wave functions*

$$\mathbf{u}(\phi;\mathbf{r}) = \exp(-j\mathbf{k}_\phi^{\mathsf{T}}\mathbf{r})\mathbf{u}_\phi; \quad \mathbf{k}_\phi = k\begin{bmatrix}\cos(\phi)\\ \sin(\phi)\\ 0\end{bmatrix}, \quad \mathbf{u}_\phi = \begin{bmatrix}\sin(\phi)\\ -\cos(\phi)\\ 0\end{bmatrix}$$

*using azimuth angles $\phi_{1,2} = 15°,\ 40°$. Figure 24 plots the summation of the two cosine fields at $f_C =$ 300 MHz. Figure 25 reports the 2-D Gaussian spline based on this rectangular grid of Figure 20. Both components $E_1$ and $E_2$ of the electric field are recovered with reasonable accuracy. Figure 26 reports distortions in the cubic spline*

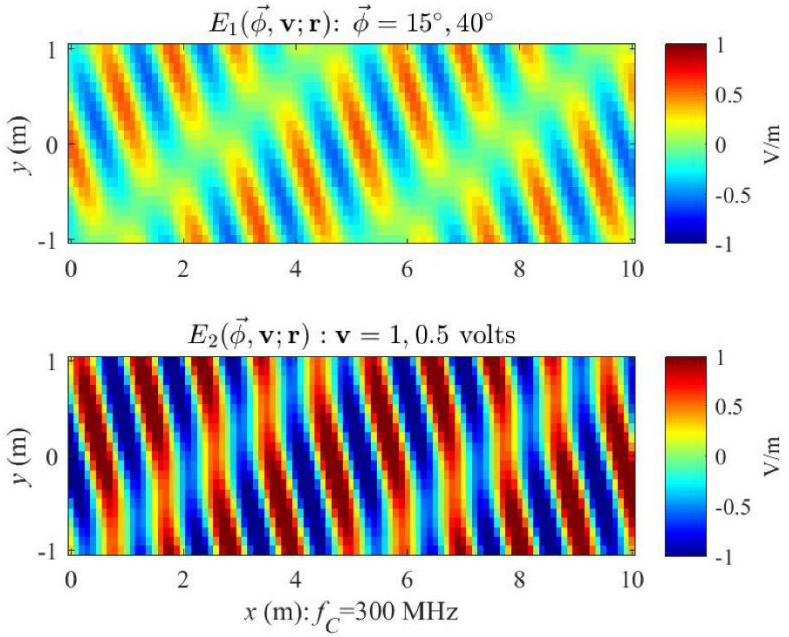


Figure 24. Summation of two plane-wave electric fields propagating at $15°$ and $40°$ azimuth at 300 MHz.

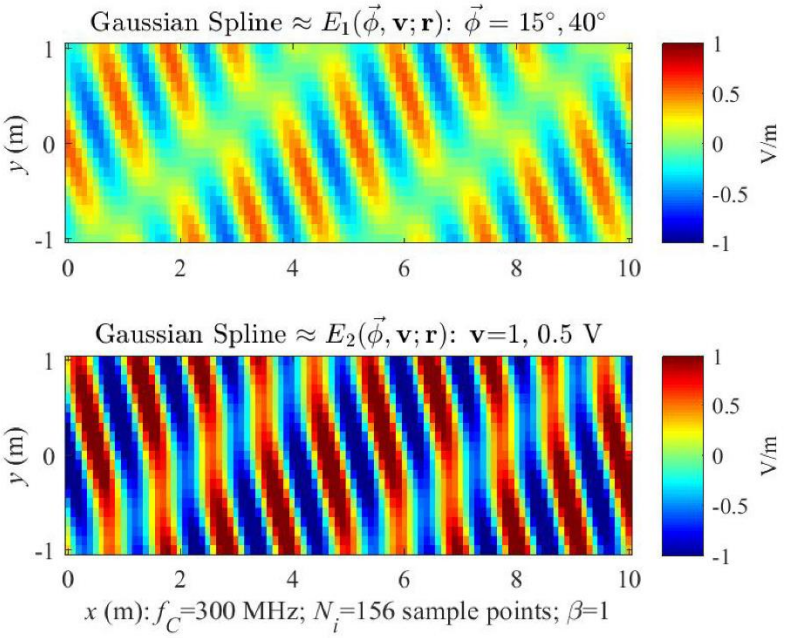


Figure 25. 2-D Gaussian spline of the two-component electric field.

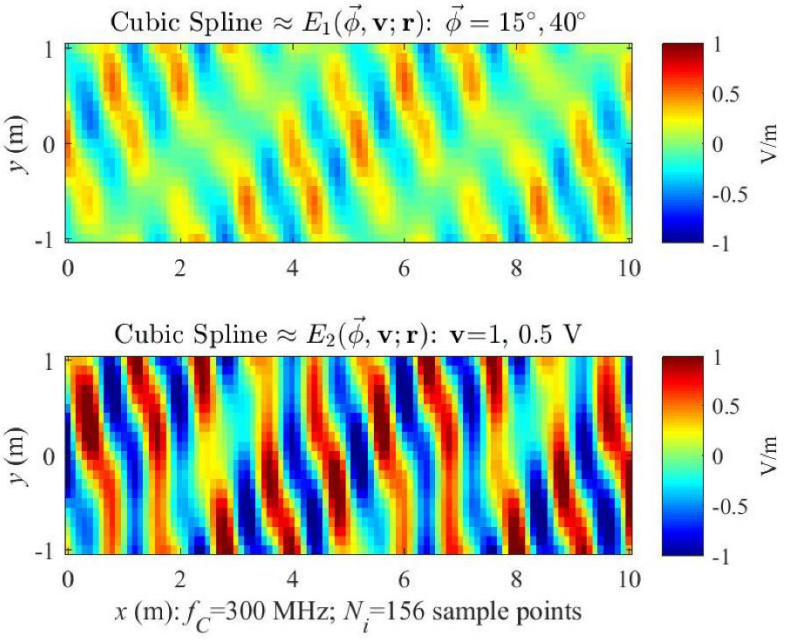


Figure 26. Cubic spline of the two-component electric field.

Example 4 employs 2-D splines interpolating the electric field components $\{E_1(\mathbf{r}_n)\}$ and $\{E_2(\mathbf{r}_n)\}$ on the rectangular grid of sample points $\{\mathbf{r}_n\}$ in Figure 20. For concreteness, the following Matlab code fragment makes explicit the linear and cubic splines of the electric field using these grid points.

```
% Cubic spline
e1Spline = interp2( xI, yI, e1I, X, Y, 'cubic' );
e2Spline = interp2( xI, yI, e2I, X, Y, 'cubic' );
```

**Summary:** These 2-D examples show that the Gaussian splines—enforcing the divergence constraint—recover the 2-D electric fields using fewer samples than the linear, natural, or cubic splines on both randomly scattered sample points and on a rectangular grid. The Matlab code that generates Example 1 is listed in Appendix A.

### 3.3 SPLINES OF 3-D PLANE WAVES

This section applies the 3-D Gaussian splines to plane-wave electric fields propagating in three dimensions. This example shows that the 3-D Gaussian splines recover the electric field using fewer samples that the standard splines. Figure 27 show the geometry for two plane-wave electric fields $\mathbf{E}_0(\mathbf{r})$ and $\mathbf{E}_1(\mathbf{r})$ propagating in the $x$-$y$-$z$ coordinate system determined by their wave vectors $\mathbf{k}_0$ and $\mathbf{k}_1$, respectively.

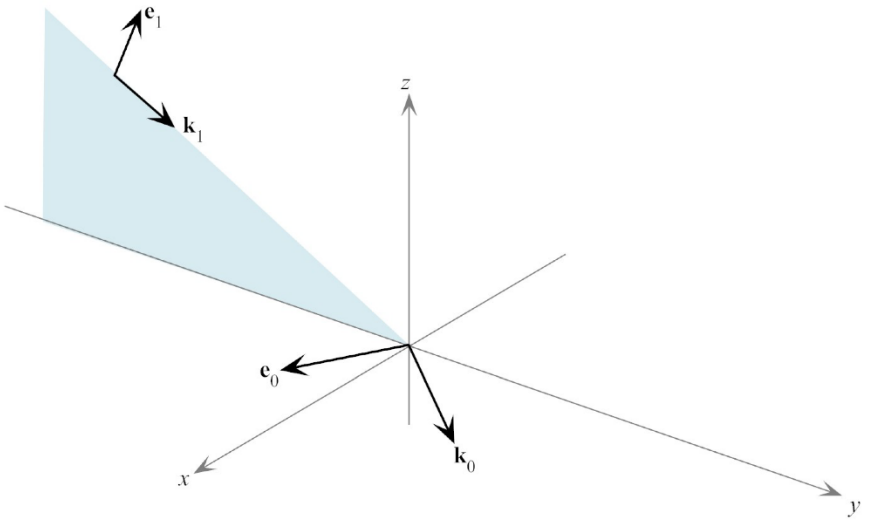


Figure 27. Propagation geometry for the sum of plane-wave electric fields $\mathbf{E}_0(\mathbf{r})$ and $\mathbf{E}_1(\mathbf{r})$; $\mathbf{k}_0$ propagates $\mathbf{E}_0(\mathbf{r})$ in the horizontal plane, $\mathbf{k}_1$ propagates $\mathbf{E}_1(\mathbf{r})$ in the vertical $y$-$z$ plane.

The electric field is the sum of the two plane waves:

$$\mathbf{E}(\mathbf{r}) = \mathbf{E}_0(\mathbf{r}) + \mathbf{E}_1(\mathbf{r}) \quad [\mathrm{V/m}].$$

The plane-wave electric field $\mathbf{E}_0$ propagating in the $x$-$y$ plane is

$$\mathbf{E}_0(\mathbf{r}) = \cos(\mathbf{k}_0^{\mathsf{T}}\mathbf{r})\mathbf{e}_0 \quad [\mathrm{V/m}]$$

with wave vector

$$\mathbf{k}_0 = k_0 \begin{bmatrix} \cos(\phi_0) \\ \sin(\phi_0) \\ 0 \end{bmatrix}; \quad k_0 = \frac{2\pi}{\lambda} \quad [\mathrm{rad/m}]$$

and direction vector

$$\mathbf{e}_0 = \begin{bmatrix} \sin(\phi_0) \\ -\cos(\phi_0) \\ 0 \end{bmatrix} \quad [\mathrm{V/m}].$$

The plane-wave electric field $\mathbf{E}_1$ propagating in the $y$-$z$ plane is

$$\mathbf{E}_1(\mathbf{r}) = \cos(\mathbf{k}_1^{\mathsf{T}}\mathbf{r})\mathbf{e}_1 \quad [\mathrm{V/m}]$$

with wave vector

$$\mathbf{k}_1 = k_1 \begin{bmatrix} 0 \\ \sin(\theta_1) \\ \cos(\theta_1) \end{bmatrix}; \quad k_1 = \frac{2\pi}{\lambda}$$

and direction vector

$$\mathbf{e}_1 = \begin{bmatrix} 0 \\ -\cos(\theta_1) \\ \sin(\theta_1) \end{bmatrix} \quad [\mathrm{V/m}].$$

The center frequency is set to $f_C = 300$ MHz or, equivalently, the wavelength is $\lambda = 1$ meter. Figure 28 plots the electric field components of

$$\mathbf{E}(\mathbf{r}) = \begin{bmatrix} E_x(\mathbf{r}) \\ E_y(\mathbf{r}) \\ E_z(\mathbf{r}) \end{bmatrix} \quad [\mathrm{V/m}]$$

on the horizontal slice at $z = 0$:

$$\mathbf{r} = \begin{bmatrix} x \\ y \\ 0 \end{bmatrix} \quad [\text{meters}]$$

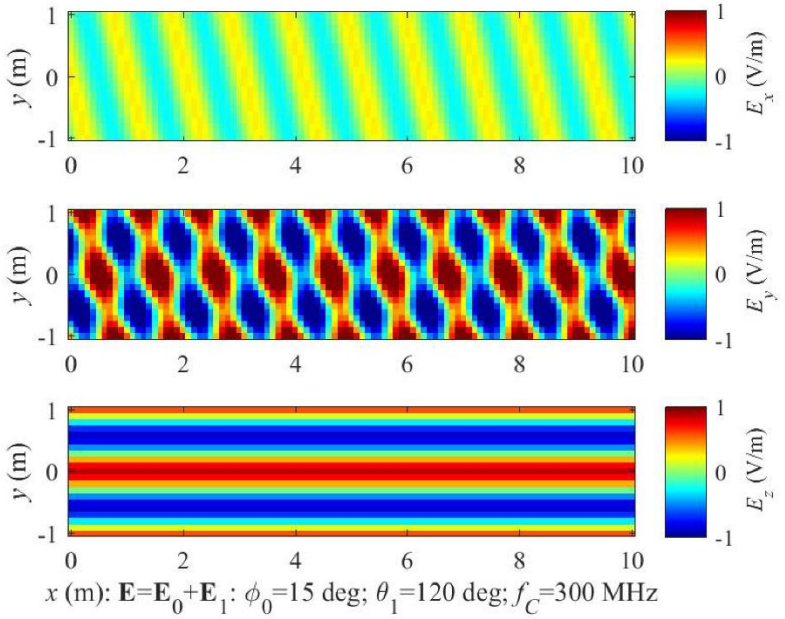


Figure 28. 3-D electric field $\mathbf{E}_0 + \mathbf{E}_1$ at 300 MHz.

Figure 29 shows the location of randomly scattered sample points $\{\mathbf{r}_n\}$ for the Gaussian spline. The 156 random samples imply a sampling density of

$$\rho = \frac{156}{2 \times 10} \approx 8 \quad [\mathrm{samples/m^2}].$$

Figure 30 shows the electric field approximation produced by the 3-D Gaussian spline based on these randomly scattered sample points. All three components of the electric field are recovered with reasonable accuracy. Some distortion is visible where the randomly scattered samples are less dense.

Figures 31, 32, and 33 separately apply each spline to the three electric field components $E_x$, $E_y$ and $E_z$ using the randomly scattered sample points of Figure 29. These splines do not force the divergence constraint and these splines do not recover the electric field. The following fragment of the Matlab code makes explicit that natural spline is applied separately to the sampled electric-field components to produce Figure 32:

```
% 6. Natural spline
e1Spline = scatteredInterpolant( xI(:), yI(:), V(1,:)', 'natural' );
e1Nat    = e1Spline(X,Y);
e2Spline = scatteredInterpolant( xI(:), yI(:), V(2,:)', 'natural');
```

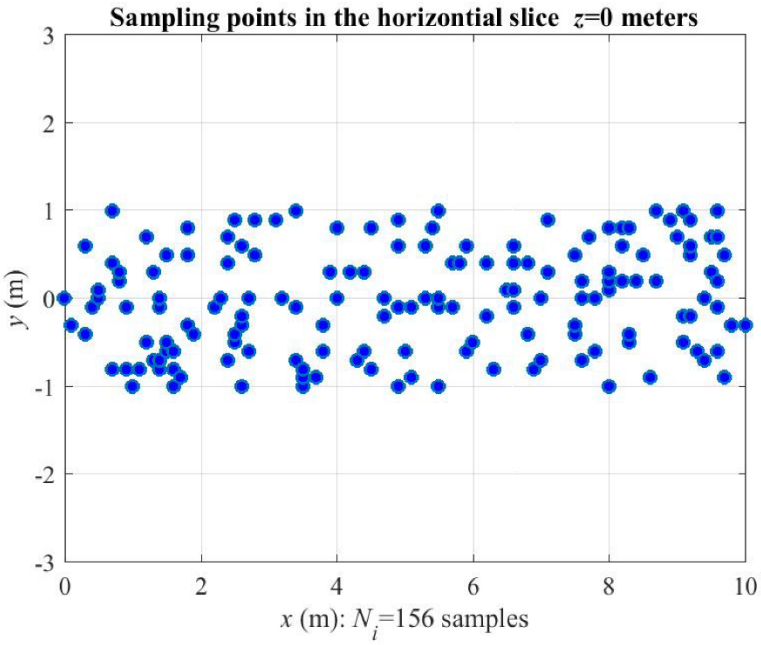


Figure 29. Randomly scattered sample points in the horizontal plane.

```
e2Nat     = e2Spline(X,Y);
e3Spline = scatteredInterpolant( xI(:), yI(:), V(3,:)', 'natural');
e3Nat     = e3Spline(X,Y);
```

Likewise, the following fragment of the Matlab code shows that the cubic spline separately interpolation the electric-field components to produce Figure 33:

```
% 5. Cubic spline
e1Cubic = griddata( xI(:), yI(:), V(1,:)', X, Y, 'cubic' );
e2Cubic = griddata( xI(:), yI(:), V(2,:)', X, Y, 'cubic');
e3Cubic = griddata( xI(:), yI(:), V(3,:)', X, Y, 'cubic');
```

**Summary:** This 3-D example shows that the Gaussian splines—enforcing the divergence constraint—recovers this 3-D electric field using fewer samples than the linear, natural, or cubic splines.

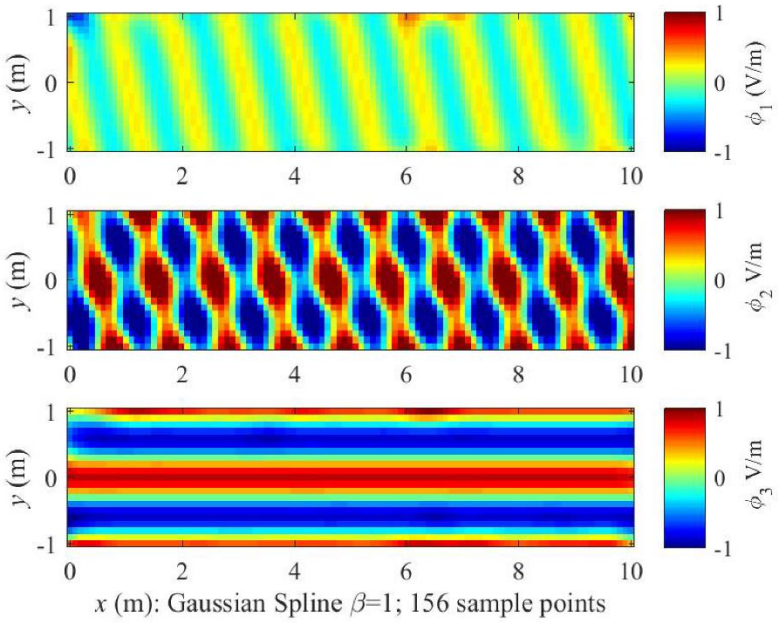


Figure 30. Gaussian spline of the 3-D electric field.

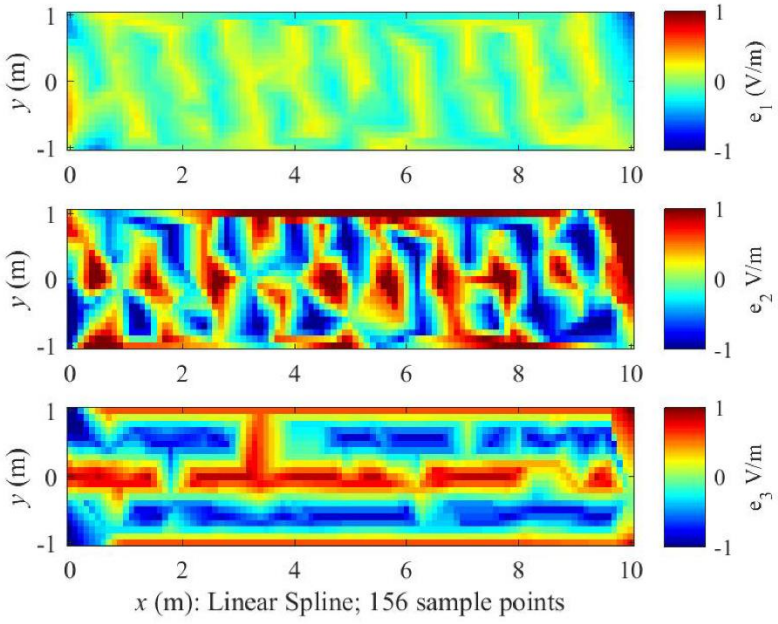


Figure 31. Linear spline applied to each component of the 3-D electric field.

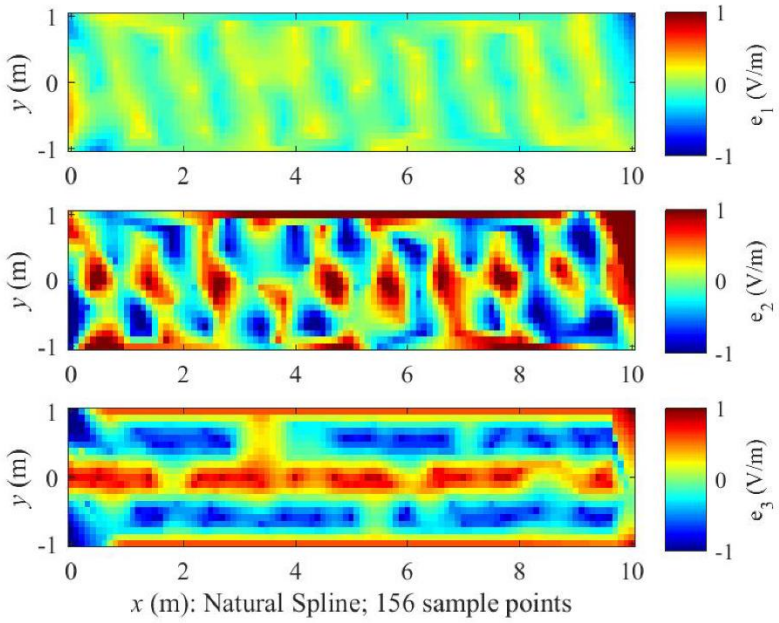


Figure 32. Natural spline applied to each component of the 3-D electric field.

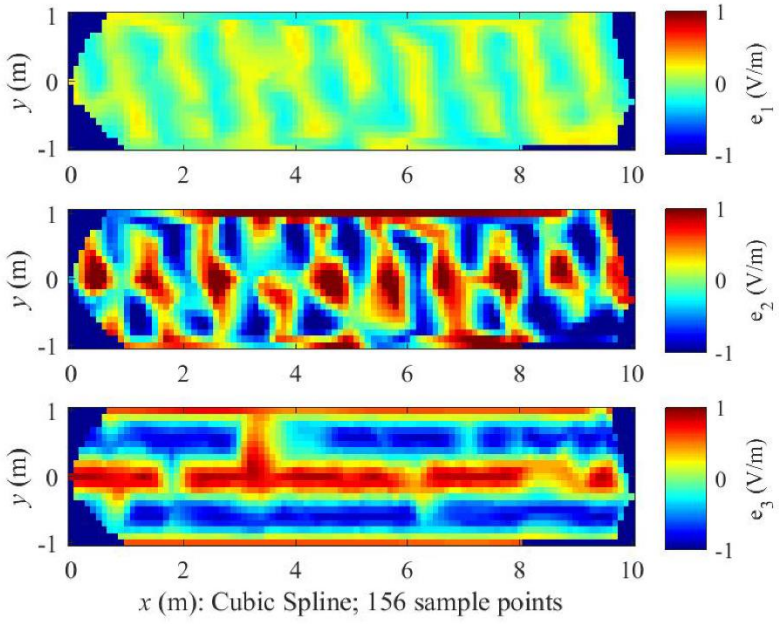


Figure 33. Cubic spline applied to each component of the 3-D electric field.

# 4. SPLINES OF THE HERTZIAN DIPOLE

This section splines the electric field produced by the Hertzian dipole. Section 4.1 reviews the Hertzian dipole in free space and verifies the vanishing of the divergence directly from the electric field. Section 4.2 approximates the electric field produced by the Hertzan dipole above a Perfect Electrical Conductor (PEC) and verifies the divergence-free Gaussian splines are better interpolants than the cubic, natural, and linear splines.

## 4.1 HERTZIAN ELECTRIC DIPOLE IN FREE SPACE

Figure 34 illustrates spherical coordinates around a short antenna carrying a vertical current $i_A$ in free space on a wire of length $\ell_A \ll \lambda$.

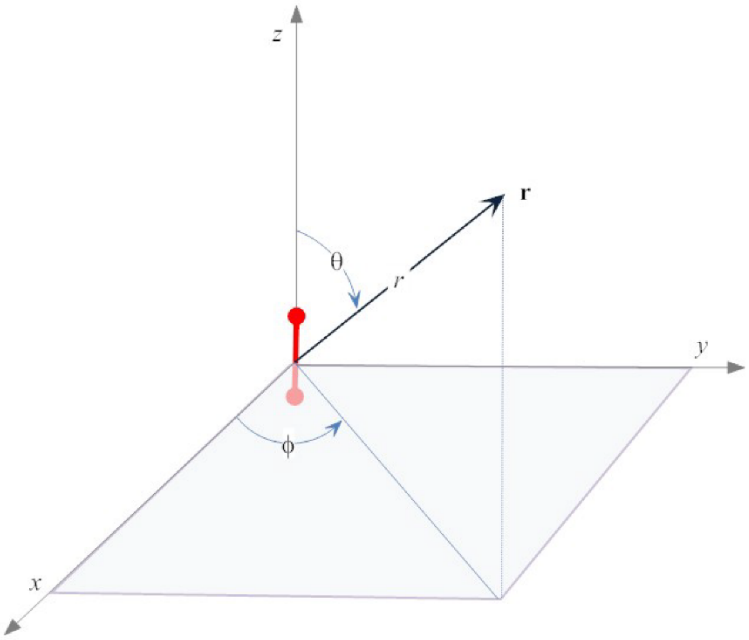


Figure 34. Hertzian dipole in spherical coordinates.

Figure 35 illustrates the electric-field components in spherical coordinates. In this coordinate system, the nonzero magnetic and electric fields of the Hertzian dipole have only three non-zero components [5, Section 17.3]:

$$H_\phi(r,\theta,\phi) = i_A \ell_A \frac{k^2}{4\pi} \sin(\theta) e^{-jkr} \left\{ \frac{j}{kr} + \frac{1}{(kr)^2} \right\}, \tag{7}$$

$$E_r(r,\theta,\phi) = i_A \ell_A \frac{\eta k^2}{2\pi} \cos(\theta) e^{-jkr} \left\{ \frac{1}{(kr)^2} - \frac{j}{(kr)^3} \right\}, \tag{8}$$

$$E_\theta(r,\theta,\phi) = i_A \ell_A \frac{\eta k^2}{4\pi} \sin(\theta) e^{-jkr} \left\{ \frac{j}{kr} + \frac{1}{(kr)^2} - \frac{j}{(kr)^3} \right\}, \tag{9}$$

where the free-space impedance $\eta = 120\pi$ ohms [5, Section 17.2] and

$$k = \frac{2\pi}{\lambda} \quad [\text{rad/m}]$$

is the wavenumber.

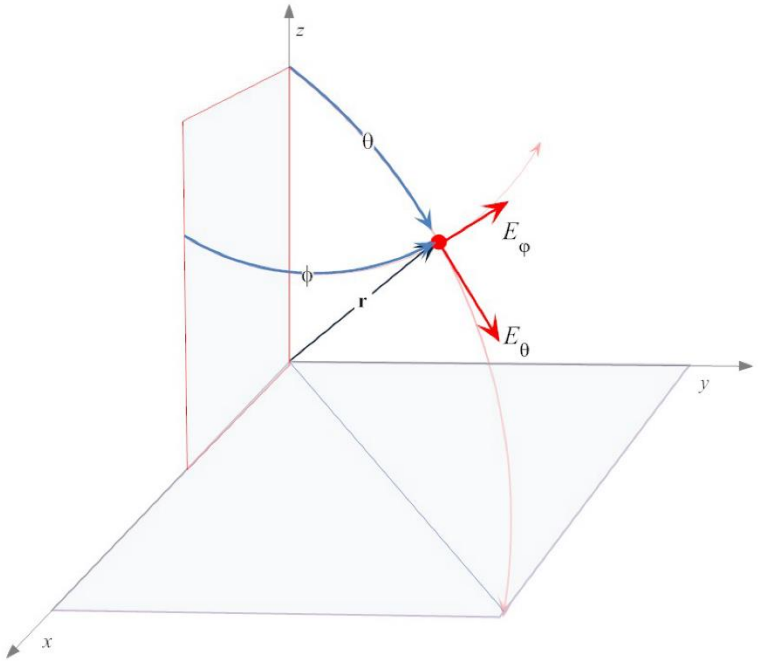


Figure 35. Spherical coordinates for the electric field.

**Example 5 (Hertzian Dipole at 300 MHz)** *Figure 36 and 37 show $E_r$ and $E_\theta$ for a vertical dipole of length*

$$\ell_A = \frac{\lambda}{10} = 0.1 \quad (\text{m})$$

*carrying $i_A = 1$ amp. Both figures show the cardioid shaping by the sine and cosine with the far field dominated by $E_\theta$.*

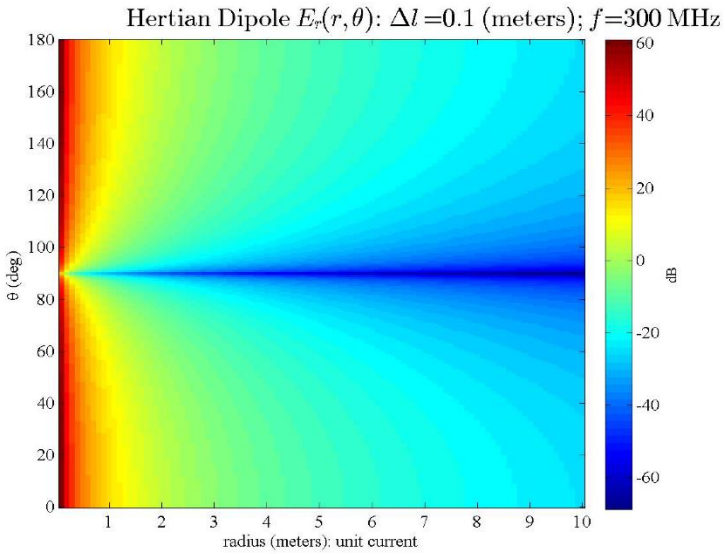


Figure 36. $|E_r(r,\theta,\phi)|^2$ (dB): $i_A = 1$ (A), $\ell_A = \lambda/10$ (m).

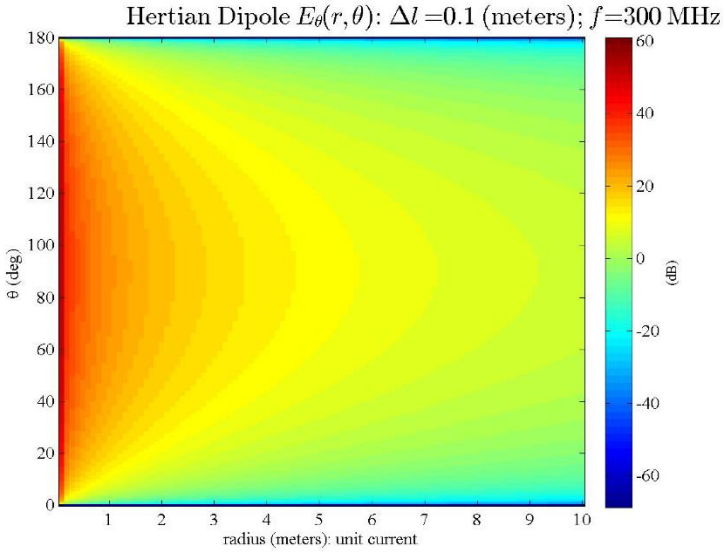


Figure 37. $|E_\theta(r,\theta,\phi)|^2$ (dB): $i_A = 1$ (A), $\Delta\ell = \lambda/10$ (m).

The divergence operator in spherical coordinates is [1, Eq. 2.31], [5, Section 4.2]

$$\nabla^{\mathsf{T}}\mathbf{A} = \frac{1}{r^2}\frac{\partial}{\partial r}\left(r^2 A_r\right) + \frac{1}{r\sin(\theta)}\frac{\partial}{\partial \theta}\left(\sin(\theta)A_\theta\right) + \frac{1}{r\sin(\theta)}\frac{\partial A_\phi}{\partial \phi}.$$

The magnetic field is easiest to verify zero divergence. Equation 7 reports that only $H_\phi$ is non-zero and also not dependent on $\phi$ so that

$$\nabla^{\mathsf{T}}\mathbf{H} = \frac{1}{r\sin(\theta)}\frac{\partial H_\phi}{\partial \phi} = 0.$$

The electric field is amenable to symbolic verification of zero divergence.

**Example 6 (Symbolic Divergence)** *This following Matlab code fragment verifies that the electric field of the Hertzian dipole given by $E_r$ (Equation 8) and $E_\theta$ (Equation 9) has zero divergence:*

```
% Electric Field: observe that the eR component has a constant
% term that is twice the eT component
syms r theta phi k positive
eR = 2*cos(theta)*exp(-j*k*r)*(  (k*r)^-2 - j*(k*r)^-3 );
eT =   sin(theta)*exp(-j*k*r)*(  j*(k*r)^-1 + (k*r)^-2 - j*(k*r)^-3);

% Divergence in spherical coordinates
divE = r^-2 * diff( r^2*eR,r) + (r*sin(theta))^-1 *diff( sin(theta)*eT, theta);

>> simplify(divE)

ans =

0
```

The sum of Hertzian dipoles is also divergence free. However, the classic examples of electric-field theory approximate the array's electric using only single Hertzian dipole shaped by an *array factor* as follows. If $\mathbf{E}_n(\mathbf{r})$ denotes the electric field produced by a Hertzian dipole at location $\mathbf{r}_n$ and $\mathbf{E}_0(\mathbf{r})$ denotes the electric field produced by a Hertzian dipole the origin, the array's far field is approximated as

$$\sum_{n=1}^{N} \mathbf{E}_n(\mathbf{r}) \approx h_{\mathrm{AF}}(\theta,\phi)\mathbf{E}_0(\mathbf{r}),$$

where the array factor $h_{\mathrm{AF}}(\theta,\phi)$ depends only on the direction to $\mathbf{r}$. Although this far-field approximation is not divergence free, its divergence tends to zero at $\mathbf{r}$ gets large. The next section shows the Gaussian splines still outperform the standard splines on these approximate fields.

### 4.2 HERTZIAN DIPOLE OVER A PERFECT ELECTRICAL CONDUCTOR

Figure 38 is a vertical cross section showing a short antenna carrying a vertical current $i_A$ over a Perfect Electrical Conductor (PEC) on a wire of length $\ell_A \ll \lambda$.

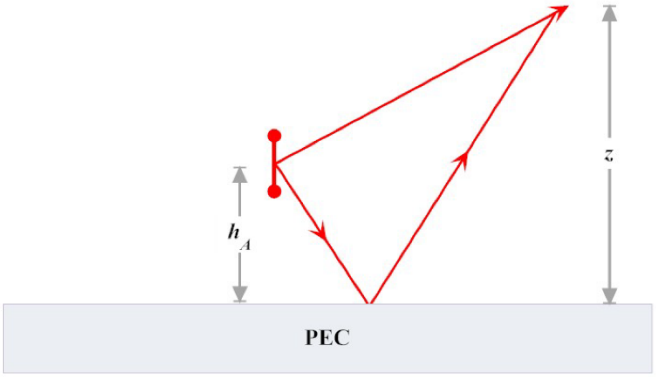


Figure 38. Hertzian dipole over PEC ground plane showing the direct and reflected rays.

The electric fields of this Hertzian dipole admit the following approximation obtained by the virtual source argument [5, Section 17.3], [2, Section 4.7.2]

$$\begin{aligned} E_r(r,\theta,\phi) &\approx i_A \ell_A \frac{\eta k^2}{2\pi} \cos(\theta) e^{-jkr} \left\{ \frac{1}{(kr)^2} - \frac{j}{(kr)^3} \right\} h_{\mathrm{AF}}(\theta), \\ E_\theta(r,\theta,\phi) &\approx i_A \ell_A \frac{\eta k^2}{4\pi} \sin(\theta) e^{-jkr} \left\{ \frac{j}{kr} + \frac{1}{(kr)^2} - \frac{j}{(kr)^3} \right\} h_{\mathrm{AF}}(\theta), \end{aligned}$$

where the *array factor* is found in [2, Eq. 4-99]

$$h_{\mathrm{AF}}(\theta) = 2\cos(kh_A \cos(\theta)),$$

and $h_A$ is the height of the dipole shown in Figure 38.

**Example 7 (Hertzian Dipole at 300 MHz over PEC)** *Referring to Figure 38, let a vertical Hertzian dipole be placed $h_A = 10$ meters above the origin and broadcast into the free space above the PEC. The dipole's length is*

$$\ell_A = 0.1 \quad [\mathrm{m}]$$

*and carries a current $i_A = 2$ amps. Figure 39, 40, and 41 show the magnitude of $E_x$, $E_y$, and $E_z$ sliced at $z = 100$ meters above the PEC.*

On the horizontal slice at $z = 100$ meters, the electric field is dominated by

$$E_\theta(r,\theta,\phi) \approx i_A \ell_A \frac{\eta k^2}{4\pi} \sin(\theta) \frac{j e^{-jkr}}{kr} h_(\theta).$$

This electric field component, restricted to this slice, points outward and down as shown in Figure 35. Consequently, the $x$-component of this field on this slice has maximal response along the $x$-axis and zero response along the $y$-axis. Figure 39 shows that $E_x$ on this slice has the radial symmetry around the origin with maximum and minimum along the $x$ and $y$ axis. Likewise, the $y$-component of this field, on this slice, has maximal response along the $y$-axis and zero response along the $x$-axis as shown in Figure 40. The lobing on both figures is caused by the interference between the two rays (See Figure 38). Figure 41 shows $z$-component of this field on the slice that captures the spherical symmetry of the electric field.

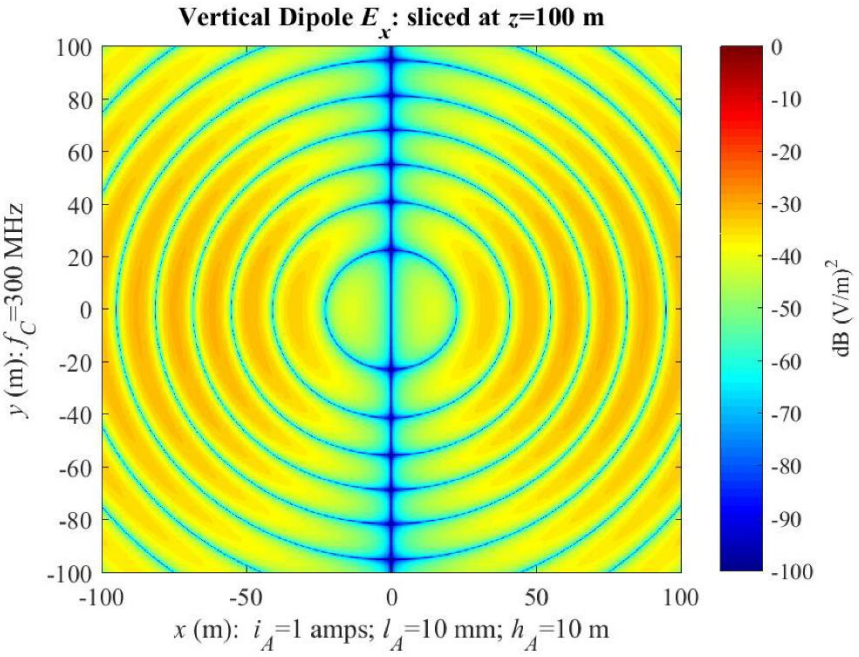


Figure 39. $|E_x(x, y, z)|^2$ at $z = 100$ meters for the Hertzian dipole over PEC.

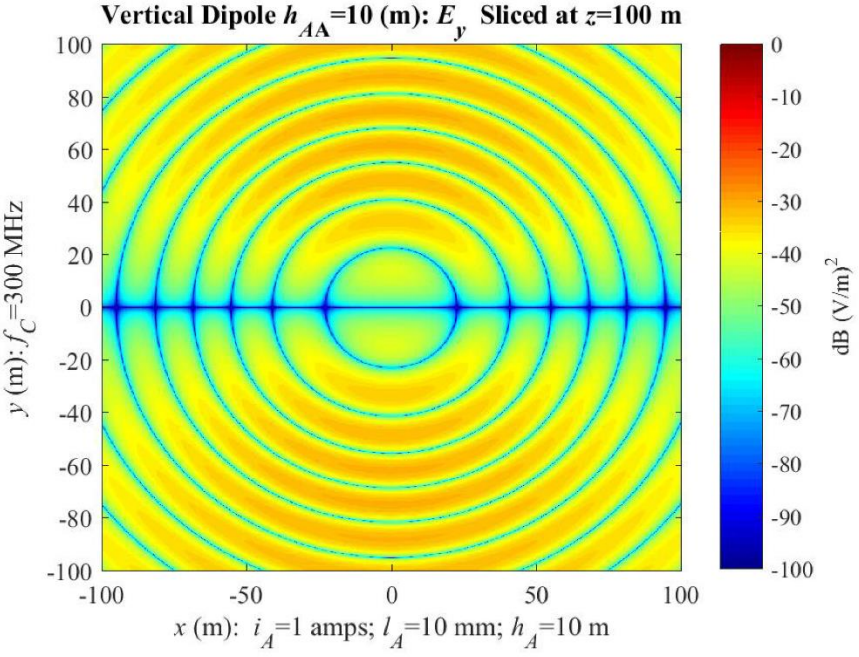


Figure 40. $|E_y(x, y, z)|^2$ at $z = 100$ meters for the Hertzian dipole over PEC.

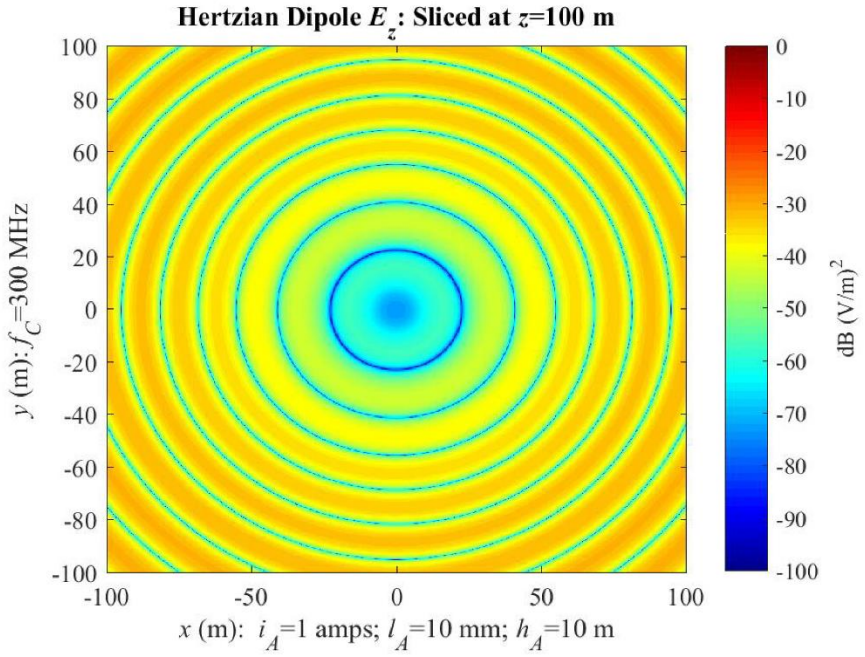


Figure 41. $|E_z(x, y, z)|^2$ at $z = 100$ meters for the Hertzian dipole over PEC.

These plots of the electric field magnitudes do not show the rapid interference patterns in the real and imaginary parts. Figure 42 plots the real part $\Re[E_x]$ on this $z = 100$ meter slice. The figure shows rapid oscillations. Interpolation of the real part of $\Re[E_x]$, $\Re[E_y]$, and $\Re[E_z]$ is the test case for the Gaussian, linear, and cubic splines.

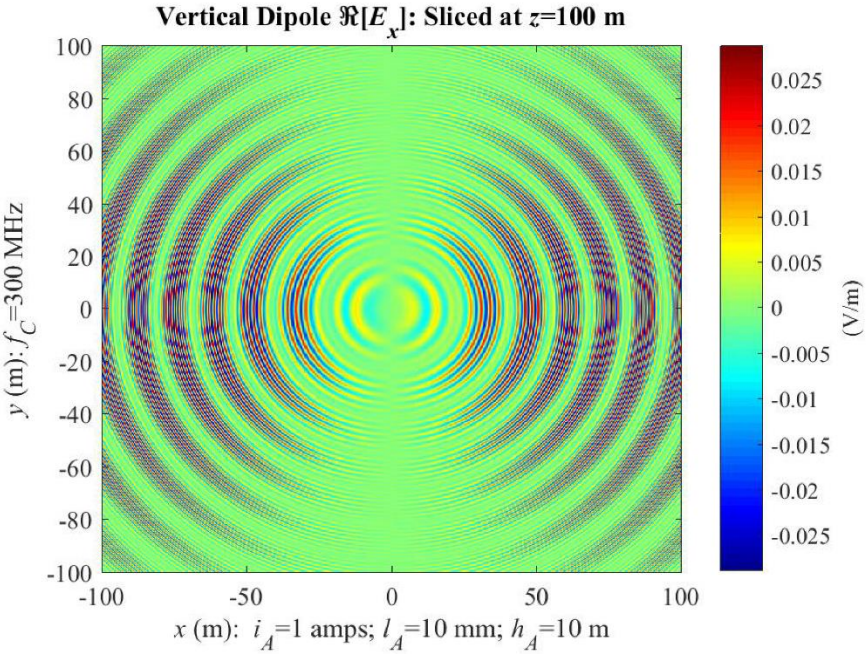


Figure 42. $\Re[E_z(x, y, z)]$ at $z = 100$ meters for the Hertzian dipole over PEC.

Figure 43 shows the real part of the electric field components $\Re[E_x]$, $\Re[E_y]$, and $\Re[E_z]$ on the horizontal strip along the $x$ axis at $z = 100$ meters. The maximum energy $\Re[E_x]$ and the weakest energy in $\Re[E_y]$ is consistent with the previous discussion. Figure 44 shows that the Gaussian spline produces almost perfect recovery of all three fields using a random sampling density of

$$\rho = \frac{1887}{20 \times 50} \approx 2 \quad [\text{samples/m}^2].$$

Figures 45 and 46 show that the linear and cubic splines deliver relatively poor recovery.

**Summary:** The Gaussian splines, by enforcing the divergence constraint, recover the relatively complex electric field of a Hertzian dipole over a PEC using fewer samples than the linear or cubic splines.

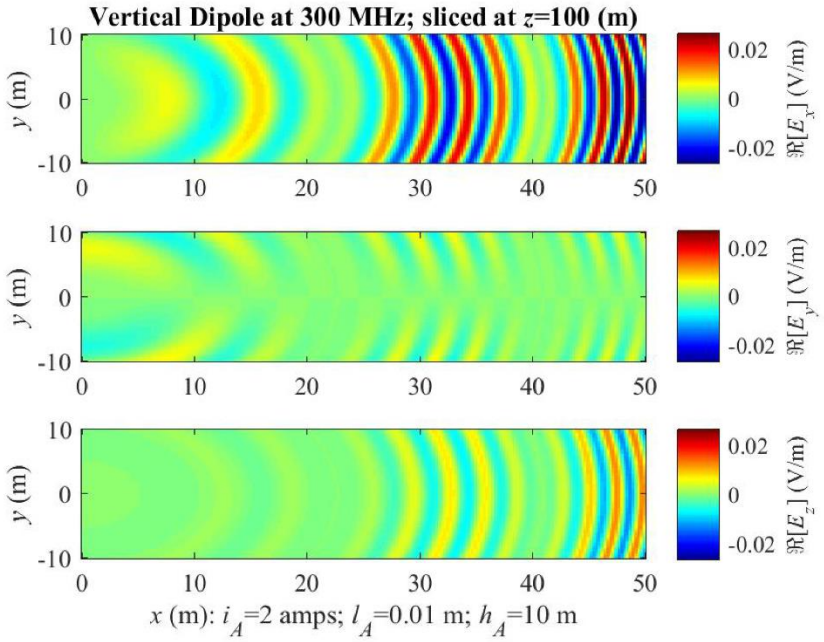


Figure 43. Real components of the electric field at $z = 100$ meters for the Hertzian dipole over PEC.

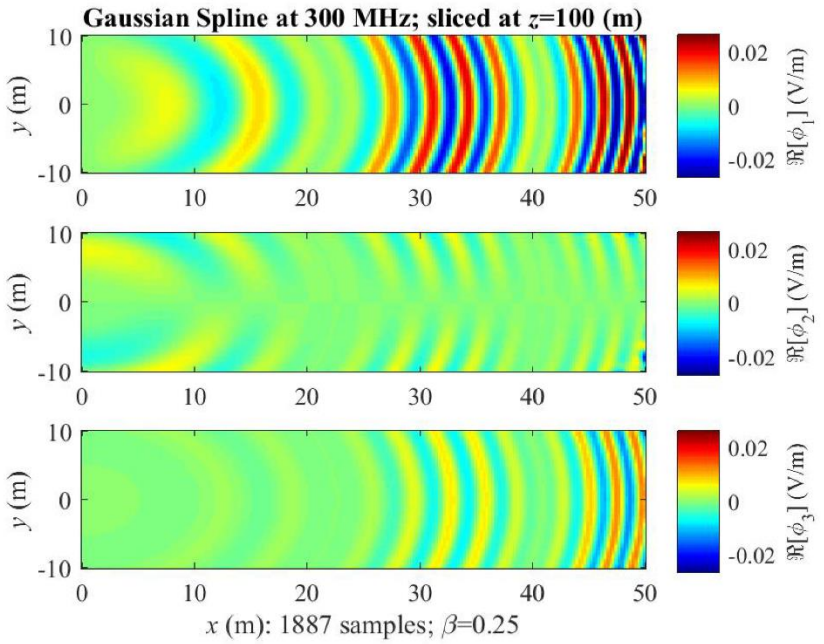


Figure 44. Gaussian spline interpolation of the real components.

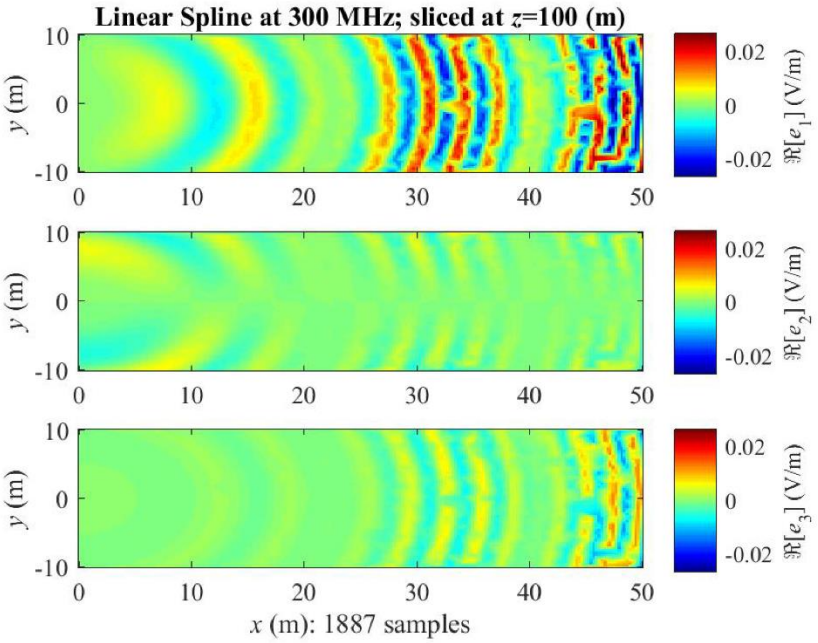


Figure 45. Linear spline of each real component.

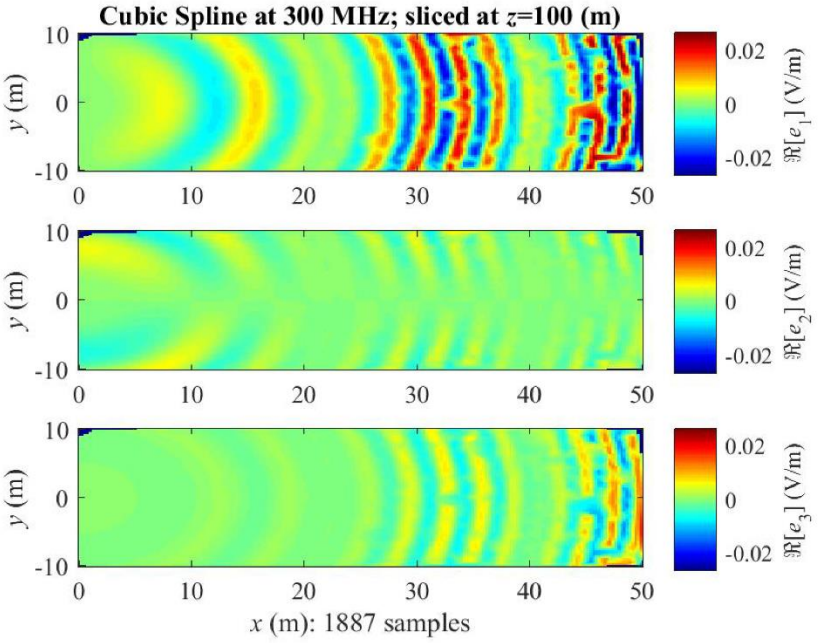


Figure 46. Cubic spline of each real component.

## 5. FLIGHT-DECK MEASUREMENTS: MAGNITUDE-ONLY

This section applies the prototype Gaussian splines to the magnitude-only measurements on the flight deck. The problem is that the Gaussian spline requires the electric field vector at each sample point $\mathbf{r}_n$

$$\mathbf{E}(\mathbf{r}_n) = \begin{bmatrix} E_x(\mathbf{r}_n) \\ E_y(\mathbf{r}_n) \\ E_z(\mathbf{r}_n) \end{bmatrix}$$

whereas the flight-deck measurements only contain the magnitudes:

$$|v_n| = \sqrt{|E_x(\mathbf{r}_n)|^2 + |E_y(\mathbf{r}_n)|^2 + |E_z(\mathbf{r}_n)|^2}.$$

This section addresses this loss of vector and phase information by working through a sequence of electric-field models of increasing complexity. Figure 47 shows the standard cubic spline fitting these magnitude-only measurements. The discussion is facilitated by letting $\psi_{\mathrm{dB}}$ denote this cubic spline obtained by fitting the magnitude measurements in dB.

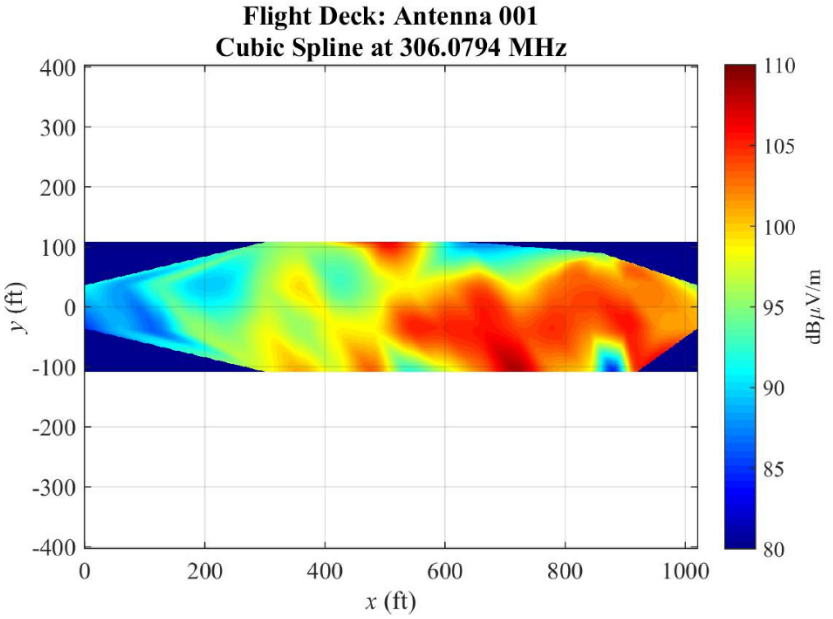


Figure 47. Cubic spline $\psi_{\mathrm{dB}}$ of the flight-deck measurements in dB.

**Remark:** Measurements imply a three-antenna system that is calibrated to map the received voltages into a 3-D electric field vector. Measurements over a flight deck imply this calibrated antenna system is translated without rotation to each measurement location.

### 5.1 CONSTANT AZIMUTH

The first electric-field model assumes a planar electric field with constant azimuth $\phi$. At each sample point $\mathbf{r}_n$ with amplitude $|v_n|$, the electric field vector has direction

$$\mathbf{E}(\mathbf{r}_n) = |v_n| \begin{bmatrix} \cos(\phi) \\ \sin(\phi) \\ 0 \end{bmatrix}. \tag{10}$$

Figure 48 shows the Gaussian spline interpolating amplitude measurements and the electric field model of Equation 10 with $\phi = 0^\circ$ so that the electric field points along the $x$-axis:

$$\mathbf{E}(\mathbf{r}_n) = |v_n| \begin{bmatrix} 1 \\ 0 \\ 0 \end{bmatrix}.$$

Although this Gaussian spline $\vec{\psi}(\mathbf{r})$ interpolates the electric-field amplitudes

$$|v_m| = \vec{\psi}(\mathbf{r}_m) = \sum_{n=1}^{N} \Psi(\beta_n; \mathbf{r}_m - \mathbf{r}_n)\mathbf{w}_n,$$

the "scaling" parameters encoding the spatial correlation of the Gaussian function

$$\beta_n = \frac{1}{2\sigma^2}; \quad \psi(\mathbf{r}) = \exp\left(-\frac{x^2 + y^2}{2\sigma^2}\right)$$

are too small. Consequently, the dipoles that constitute this spline (See Figure 8) are revealed as Gaussian thumbtacks.

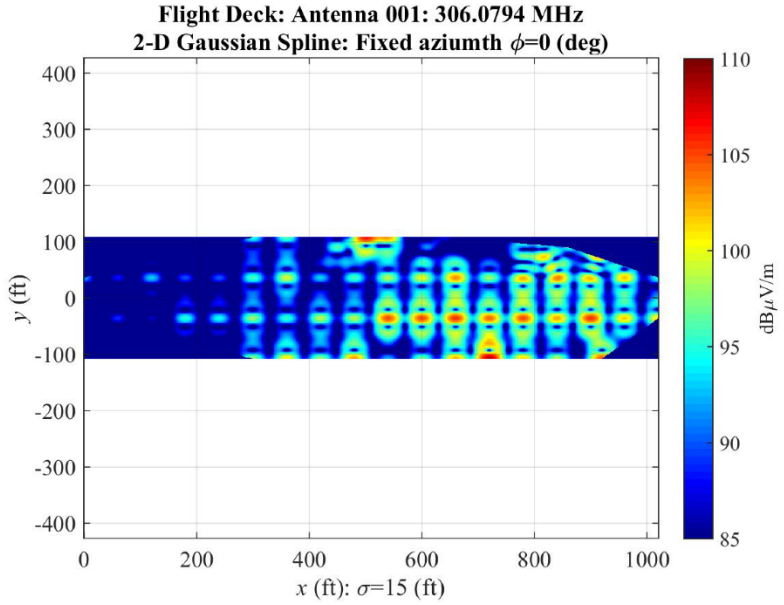


Figure 48. A "thumbtack" Gaussian spline of the flight-deck measurements; the 2-D electric field is forced to point along the $x$ axis ($\phi = 0^\circ$) with a small spatial correlation ($\sigma = 15$ feet).

Figure 49 increases the spatial correlation to $\sigma = 50$ meters. The Gaussian spline does smooth but the $x$-direction set by $\phi = 0°$ is apparent.

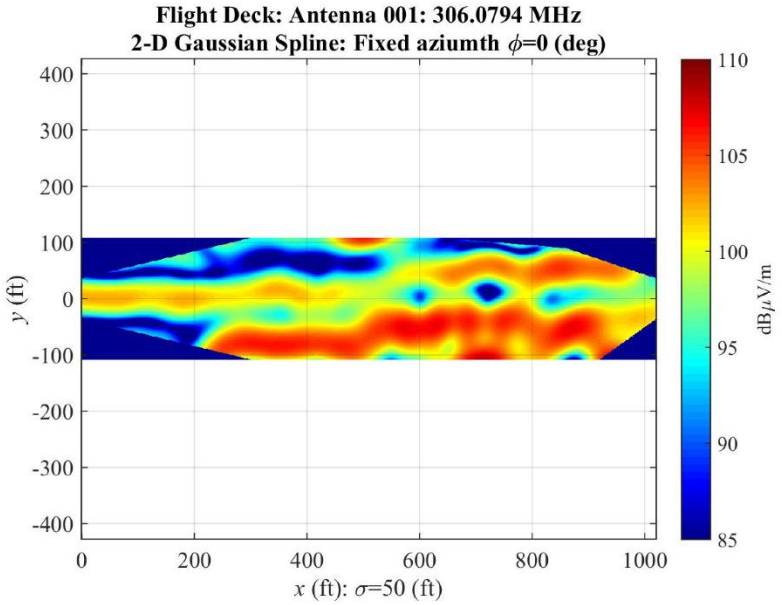


Figure 49. 2-D Gaussian spline of the flight-deck measurements; the 2-D electric field is forced to point along the $x$ axis ($\phi = 0°$) with spatial correlation $\sigma = 50$ feet.

Figure 50 turns the azimuth to $\phi = 15°$. The Gaussian spline interpolates the electric field vector of Equation 10 and better matches cubic spline $\psi_{\text{dB}}$ of Figure 47. Therefore, a natural approach seeks a divergence-free spline that is "closest" to the cubic spline of the magnitude-only measurements.

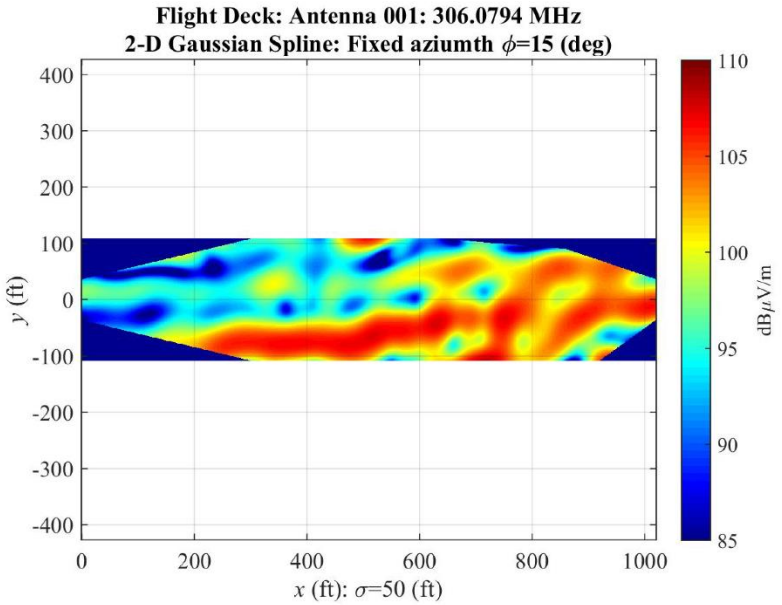


Figure 50. 2-D Gaussian spline of the flight-deck measurements; the 2-D electric field vectors all have $15°$ azimuth.

The natural approach seeks optimum azimuth $\phi$ and spatial correlation $\sigma$ to minimize the amplitude error between the cubic spline $\psi_{\rm dB}$ and the divergence-free spline over a dense sampling of the 2-D domain. At each sample point, the electric field model is parameterized by the azimuth

$$\mathbf{E}(\mathbf{r}_n) = |v_n| \begin{bmatrix} \cos(\phi_{\rm OPT}) \\ \sin(\phi_{\rm OPT}) \\ 0 \end{bmatrix} \tag{11}$$

and divergence-free spline is parameterized by the spatial correlation:

$$\vec{\psi}(\phi_{\rm OPT}, \sigma_{\rm OPT}; \mathbf{r}) := \sum_{n=1}^{N} \Psi(\beta_{\rm OPT}; \mathbf{r} - \mathbf{r}_n)\mathbf{x}_n; \quad \beta_{\rm OPT} = \frac{1}{2\sigma_{\rm OPT}^2},$$

where $\phi_{\rm OPT}$ and $\sigma_{\rm OPT}$ are minimizers of the following maximum error function:

$$\min \left\{ \left\| \psi_{\rm dB} - 10\log_{10}(\|\vec{\psi}(\phi, \sigma\|^2) \right\|_\infty : 0 \le \phi \le 90^\circ; 10 \le \sigma \le 100 \right\}.$$

Figure 51 reports local minimizers are

$$\begin{aligned} \phi_{\rm OPT} &= 10^\circ \\ \sigma_{\rm OPT} &= 49 \ \ [\text{ft}] \end{aligned}$$

The values are relatively close to the azimuth of $\phi = 15^\circ$ and spatial correlation $\sigma = 50$ feet obtained by hand (See Figure 50).

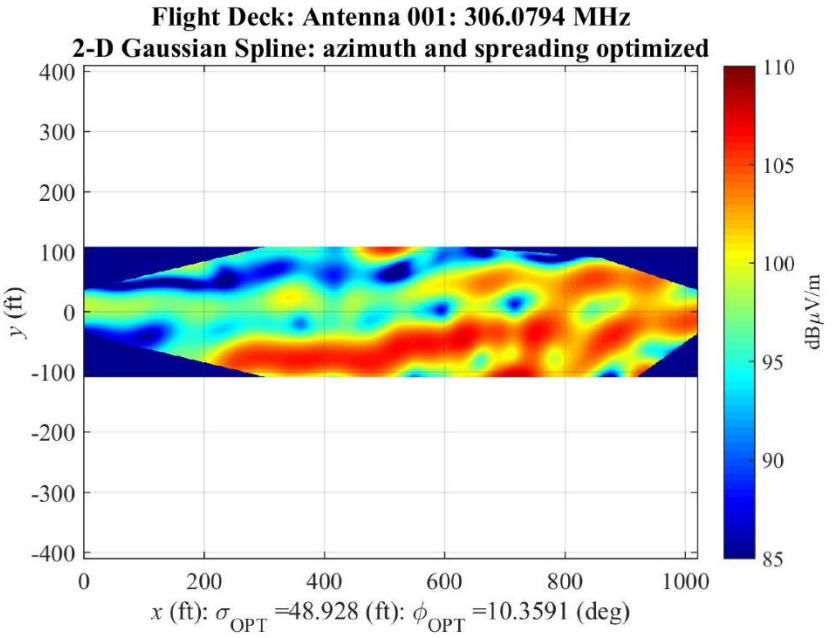


Figure 51. 2-D Gaussian spline of the flight-deck measurements; the 2-D electric field vectors all use an azimuth angle $\phi_{\rm OPT}$ and spatial correlation $\sigma_{\rm OPT}$ optimized to minimize the error from the 2-D cubic spline of Figure 47.

### 5.2 VARIABLE AZIMUTHS

The second electric-field model still constrains the electric field to a plane but varies the azimuths at each sample point:

$$\mathbf{E}(\mathbf{r}_n) = |v_n| \begin{bmatrix} \cos(\phi_n) \\ \sin(\phi_n) \\ 0 \end{bmatrix}. \tag{12}$$

Therefore, the divergence-free spline is parameterized by the azimuths $\{\phi_n\}$ while the spatial correlation $\sigma$ is held constant:

$$\begin{aligned} \vec{\psi}(\{\phi_n\}; \mathbf{r}) &= \sum_{n=1}^{N} \Psi(\beta; \mathbf{r} - \mathbf{r}_n)\mathbf{w}_n; \quad \beta = \frac{1}{2\sigma^2}, \\ \sigma &= 50 \quad [\text{ft}]. \end{aligned}$$

The azimuths $\{\phi_n\}$ are chosen to minimize the amplitude error between the cubic spline and the divergence-free spline on a dense sampling of the 2-D domain.

$$\min \left\{ \left\| \psi_{\text{dB}} - 10\log_{10}(\|\vec{\psi}(\{\phi_n\})\|^2) \right\|_\infty : 0^\circ \le \phi_n \le 360^\circ \right\}.$$

Figure 52 shows a local minimum. This spline interpolates the measured magnitudes and approximates the cubic spline $\psi_{\text{dB}}$ assuming the electric field model of Equation 12.

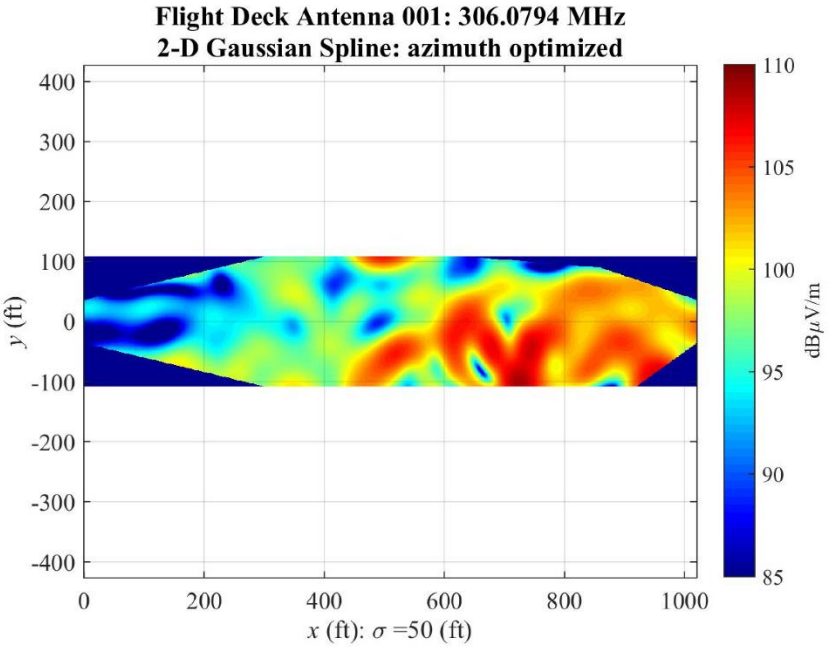


Figure 52. 2-D Gaussian spline of the flight-deck measurements; azimuths $\{\phi_k\}$ optimized to fit the cubic spline.

### 5.3 VARIABLE PHASES

The third and final electric-field model is based on the measurements of the electric field over the flight deck. These measurements employed a vertical dipole so that only $E_z$ of the electric field was measured. Therefore, the electric field is modeled in the $z$-direction having measured amplitude $|v_n|$ but an unknown voltage phase $\angle v_n$ at each sample point:

$$\mathbf{E}(\mathbf{r}_n) = |v_n| e^{j\angle v_n} \begin{bmatrix} 0 \\ 0 \\ 1 \end{bmatrix}. \tag{13}$$

Therefore, the divergence-free spline is parameterized by the voltage phases $\{\angle v_n\}$ while the spatial correlation $\sigma$ is held constant:

$$\begin{aligned} \vec{\psi}(\{\angle v_n\}; \mathbf{r}) &= \sum_{n=1}^{N} \Psi(\beta; \mathbf{r} - \mathbf{r}_n)\mathbf{w}_n; \quad \beta = \frac{1}{2\sigma^2}, \\ \sigma &= 50 \quad [\text{ft}]. \end{aligned}$$

The phases $\{\angle v_n\}$ are chosen to minimize the amplitude error between the cubic spline and the divergence-free spline on a dense sampling of the 2-D domain.

$$\min \left\{ \left\| \psi_{\text{dB}} - 10\log_{10}(\|\vec{\psi}(\{\angle v_n\})\|^2) \right\|_\infty : 0 \le \angle v_n \le 360^\circ \right\}.$$

Figure 52 plots a local minimum. This divergence-free spline interpolates the measured magnitudes and approximates the cubic spline $\psi_{\text{dB}}$ assuming the electric field model of Equation 13.

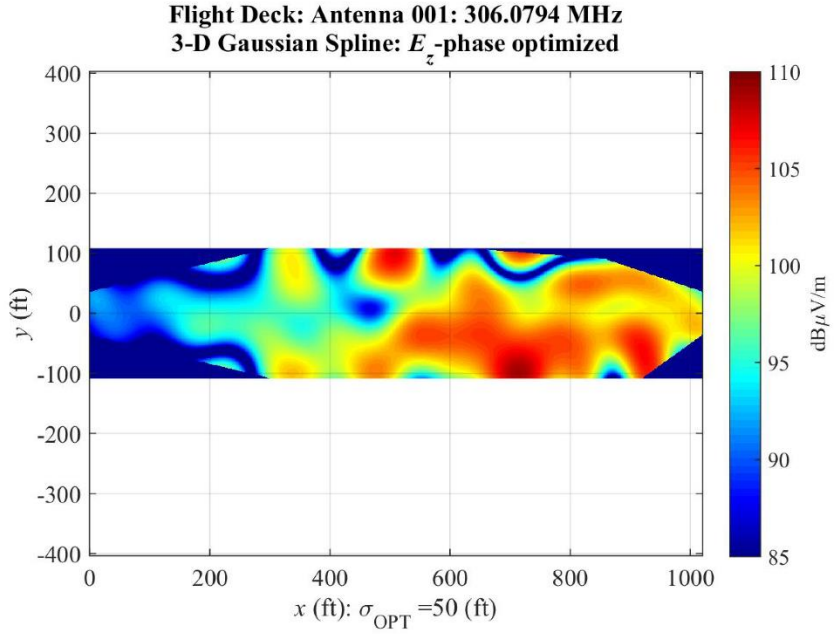


Figure 53. 3-D Gaussian spline of the flight-deck measurements; voltage phases $\{\angle v_k\}$ are optimized to fit the cubic spline.

### 5.4 SUMMARY

Figure 54 compares the cubic spline $\psi_{\mathrm{dB}}$ to the divergence-free splines $\vec{\psi}(\{\phi_n\})$ and $\vec{\psi}(\{\angle v_n\})$. All three splines show similar large-scale features. This similarity is expected because the divergence-free splines interpolate the measured magnitude of the electric field while varying their free parameters to approximate the cubic spline $\psi_{\mathrm{dB}}$. The most credible spline is $\vec{\psi}(\{\angle v_n\})$ because the modeled electric field direction is consistent with the vertical measurement antenna.

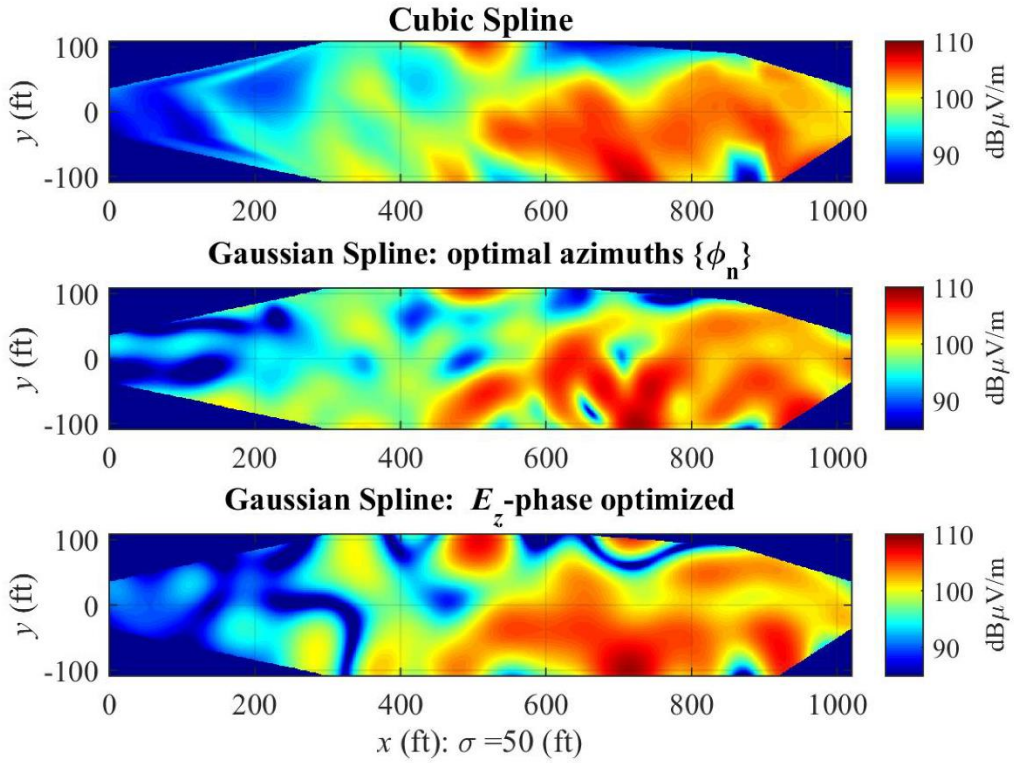


Figure 54. (Top) Cubic spline $\psi_{\mathrm{dB}}$ of the flight-deck measurements; (Middle) Gaussian spline of the flight-deck measurements optimizing azimuths $\{\phi_n\}$; (Bottom) Gaussian spline of the flight-deck measurements optimizing voltage phases $\{\angle v_k\}$.

There are other approaches to handle measurements limited by magnitude only. A classic approach optimizes the free parameters to find a divergence-free spline that minimizes the worst error obtained when omitting one or more measurements. More fruitful approaches increase the information about the electric-field vector. For example, the simplest approach employs three antennas to measure the amplitude of the electric field components:

$$|\mathbf{E}(\mathbf{r}_n)| = \begin{bmatrix} |E_x(\mathbf{r}_n)| \\ |E_y(\mathbf{r}_n)| \\ |E_z(\mathbf{r}_n)| \end{bmatrix} = \begin{bmatrix} |v_{x,n}| \\ |v_{y,n}| \\ |v_{z,n}| \end{bmatrix}. \tag{14}$$

The divergence-free splines interpolate the electric field assuming the *measurement model* of Equation 14 where the voltage amplitudes are fixed while the voltage phases are varied to find an optimal spline as in Section 5.3:

$$\mathbf{E}(\mathbf{r}_n) = \begin{bmatrix} |v_{x,n}| e^{j\angle v_{x,n}} \\ |v_{y,n}| e^{j\angle v_{y,n}} \\ |v_{z,n}| e^{j\angle v_{z,n}} \end{bmatrix}. \tag{15}$$

A more substantial approach employs three antennas to measure the complex-valued components of the electric field:

$$\mathbf{E}(\mathbf{r}_n) = \begin{bmatrix} E_x(\mathbf{r}_n) \\ E_y(\mathbf{r}_n) \\ E_z(\mathbf{r}_n) \end{bmatrix} = \begin{bmatrix} |v_{x,n}|e^{j\angle v_{x,n}} \\ |v_{y,n}|e^{j\angle v_{y,n}} \\ |v_{z,n}|e^{j\angle v_{z,n}} \end{bmatrix}. \tag{16}$$

This measurement model only requires the divergence-free spline vary the spatial correlation at each sample point. However, both measurement models imply *simultaneous* sampling of the electric-field. This simultaneous sampling assumption is implicit in both the 2-D electric fields of Section 3 and the 3-D electric fields of Section 4. Simultaneous sampling requires either multiple phase-locked receivers or an electric field that is stable over the measurements.

Flight deck measurements are currently conducted by positioning one calibrated antenna over the flight deck (See Figure 3) while broadcasting a strong continuous wave. Therefore, the sampled amplitudes are almost constant—despite the time between measurements—so that the measurement model of Equation 14 allows the phase estimation of Equation 15.

Extending these flight deck measurements to the electric-field vector challenging. A strong broadcast should force the electric-field vector to be relatively stable at each location. However, moving the equipment to each measurement location will induce location-dependent phases $\{\phi_n\}$ as modeled by Equation 16:

$$\mathbf{E}(\mathbf{r}_n) = e^{j\phi_n} \begin{bmatrix} |v_{x,n}|e^{j\angle v_{x,n}} \\ |v_{y,n}|e^{j\angle v_{y,n}} \\ |v_{z,n}|e^{j\angle v_{z,n}} \end{bmatrix}. \tag{17}$$

In this case, the divergence-free splines interpolate the electric field assuming the measurement model of Equation 16 while only the location-dependent phases $\{\phi_n\}$ need to be varied to find an optimal spline:

# 6. APPLICATIONS

The canonical example of this report originated from shipboard EMI measurements. The divergence-free Gaussian splines deliver a physics-based interpolation using these relatively sparse measurements to recover a complete electric field. Interpolating these EMI measurements is a special case of electric-field scanning. This final section sets out three applications of electric-field scanning well-suited for divergence-free splines:

- Flight-deck EMI
- Shipboard HF/VHF/UHF antenna patterns
- VLF antenna patterns

All these applications employ a small drone or quadcopter carrying a vector antenna to sample the 3-D electric field. Discussions on measurement issues close this section. The first application is the volumetric measurement of the electric field over a flight deck. A UAV sweeping above the flight deck will produce a dense sampling of this volume in a matter of minutes whereas the standard sparse sampling obtained by manually positioning a single antenna to each measurement location takes at least one full working day.

The second application measures shipboard HF/VHF/UHF antenna patterns. Measuring these patterns is a substantial task undertaken at a Shipboard Electronic Systems Evaluation Facility (SESEF) [20]:

> SESEF's are land-based test facilities, established to facilitate testing of electromagnetic transmitting and receiving equipment for U.S. Navy, U.S. Coast Guard and Military Sealift Command vessels.

The standard approach to measure the shipboard antenna radiation patterns requires [20]:

> the ship to perform a circular maneuver around a SESEF buoy or geodetic point of reference. The maneuver is required to be as circular as possible with the same angular velocity (constant turn rate approximately 18 to 20 degrees per minute, circle diameter not greater than 1 nm).

Figure 55 is a map of the SESEF range off the coast of San Diego, CA. This figure gives the size of the range and the commitment of a ship to the SESEF measurement protocol. In contrast, a UAV flying in a kilometer-sized cylinder around the ship could sample antenna patterns for interpolation by the divergence-free splines with minimal disruption to the ship's schedule, eliminate the ship's maneuver requirements, and free the ship from the SESEF range.


Figure 55. SESEF range at San Diego, CA [20].

The third application measures VLF antenna patterns [10]. Figure 56 is a map of the Cutler VLF antenna arrays. The north and south arrays each consist of 13 towers:

- A center tower,
- Six middle towers equally spaced around a circle of radius 1,825 feet centered at the center tower,
- Six outer towers equally spaced around a circle of radius 3,070 feet centered at the center tower.

The size of these VLF arrays and the long wavelength makes pattern measurements challenging [4]. A UAV flying a kilometer-sized cylinder around the arrays could sample the VLF antenna pattern for interpolation by divergence-free splines.

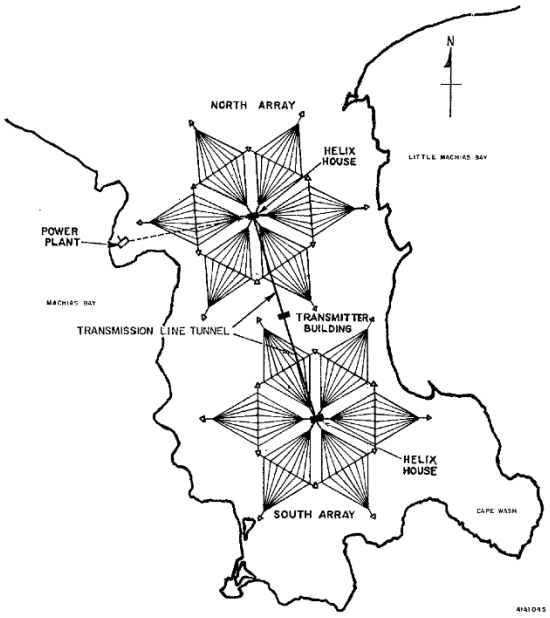


Figure 56. Culter VLF antenna arrays [10].

All these applications require the UAV to obtain a sufficiently dense sampling of the electric field with sampling locations to a appropriate accuracy, and a determination if phase is to be measured. The wavelength $\lambda$ and the complexity of the field determine the sampling density.

**Example 8 (SESEF Sampling)** *Section 4.2 reports a sampling density* $\rho = 2$ *samples per square meter when the wavelength* $\lambda = 1$ *meter for the Hertzian dipole above a PEC. If this dipole scales to HF with* $\lambda = 100$ *meters, as in a SESEF application at 3 MHz, a sampling density of 2 samples per* $100 \times 100$ *square meters could be possible. Removing the "if" in this SESEF application requires the modeling and interpolating a simple HF antenna close to the sea surface to estimate the sampling density.*

This report does not estimate the sensitivity of the Gaussian splines to noise in the measurements or errors in the measurement locations. An estimate of this sensitivity to the measurement locations is computable by perturbing the locations. For example, when a sampling density is estimated as in Example 8 and measurement locations are determined, a random perturbation of the locations will produce a different spline and an error between the splines. Varying the size of the perturbations produces an average error as a function of the location uncertainty. This curve determines the feasibility of the UAV sampling.

Measurement noise is typically handled with regularization applied to the matrix inversion of Equations 4 and 5, assuming a noise covariance matrix is available [16]. Total least squares handles both noise in the measurements and errors assuming the ideal Vandermode matrix [8]. In this application, sources of errors in the Vandermode matrix arise from both antenna calibration errors and errors in the measurement locations. Both regularization and total least squares are excellent extensions of the Gaussian splines.

This page is intentionally blank.

# REFERENCES


1. Arfken, George [1970] *Mathematical Methods for Physicists*, second edition, Academic Press, New York, NY.

2. Balanis, Constantine A. [1982] *Antenna Theory (analysis and design)*, Harper & Row, New York, NY.

3. Bostan, Emrah; Michael Unser; John Paul Ward [2015] Divergence-Free Wavelet Frames, *IEEE Signal Processing Letters*, 22(8).

4. Deneris, C. A., Schukantz, J. H., Hansen, P. M., Logan, J. C. [1994] *NEC4 Analysis of a Navy VLF Antenna*, 10th Annual Review of Progress in Computational Electromagnetics, Monterey, California. DTIC Accession Number: ADA279340.

5. Edminister, Joseph A. [1993] *Electromagnetics*, second edition, Schaum's Outline Series, McGraw-Hill, New York, NY.

6. Foresman, Pearson Scott [2018] *Archives of Pearson Scott Foresman*, donated to the Wikimedia.

7. Garrity, Thomas A. [2015] *Electricity and Magnetism for Mathematicians*, Cambridge University Press, New York, NY.

8. Golub, Gene H. & Charles F. Van Loan [1989] *Matrix Computations*, second edition, The John Hopkins University Press, Baltimore, Maryland.

9. Halliday, David & Robert Resnick [1962] *Physics: Part II*, John Wiley & Sons, Inc., New York, NY.

10. Hansen, P. M. [1994] *VLF Culter Hollow Core Cable Repair/Replacement*, Technical Report 1681, Naval Electronics Systems Command (Approved for public release; distribution is unlimited).

11. Harounaa, S. Kadri & V. Perrier [2013] Effective construction of divergence-free wavelets on the square, *Journal of Computational and Applied Mathematics*, 240, pages 74–86.

12. Hilton, David P. [2016] `UCLASS locations.xlsx`, personal communication, (Unclassified).

13. Kaiser, Gerald [1994] *A Friendly Guide to Wavelets*, Burkhäuser, Boston, MA.

14. Keller, John [2016] Navy researchers seek to tame the electromagnetic interference beast plaguing shipboard electronics, *Military & Aerospace Electronics*, https://www.militaryaerospace.com/computers/article/16715025/ navy-researchers-seek-to-tame-the-electromagnetic-interference-beast-plaguing-shipboard-electronics

15. Kim, John C. & Eugen I. Muehldorf [1995] *Naval Shipboard Communication Systems*, Prentice-Hall, Inc., Englewood Cliffs, New Jersey.

16. Luenberger, D. G. [1969] *Optimization by Vector Space Methods*, John Wiley, New York, NY.

17. Lemarie-Rieusset, Pierre-Gilles [1992] Wavelets, Splines and Divergence-Free Vector Functions, in *Approximation Theory, Spline Functions and Applications*, S. P. Singh (ed.), Kluwer Academic Publishers.

18. McNally, Colin P. [2011] Divergence-Free Interpolation of Vector Fields from Point Values—Exact $\nabla \cdot \mathbf{B} = 0$ in Numerical Solutions, *Monthly Notices of the Royal Astronomical Society: Letters*, 413(1).

19. Navikas, D.; P. Tarvydas; A. Noreika [2006] Electric Field Potential Interpolation, DOI: 10.1109/BEC.2006.311065.

20. NAVSEA [2006] *Shipboard Test Execution Manual*, NAVSEA Test and Evaluation Office (Distribution Statement "A"; Approved for Public Release; Distribution is Unlimited).

21. Sandwell, David T. [1987] Biharmonic Spline Interpolation of GEOS-3 and SEASAT Altimeter Data, *Geophysical Research Letters*, 14(2).

22. Shen, Liang Chi & Jin Au Kong [1987] *Applied Electromagnetism*, second edition, PWS Engineering, Boston, MA.

23. Stoer, J. & R. Bulirsch [1980] *Introduction to Numerical Analysis*, Springer-Verlag, New York, NY.

24. N. Sukumar, N. [1997] A Note on Natural Neighbor Interpolation and the Natural Element Method (NEM), `http://dilbert.engr.ucdavis.edu/~suku/nem`.

25. Grace Wahba [1982] *Vector Splines On The Sphere, with Application to the Estimation Of Vorticity and Divergence From Discrete, Noisy Data*, Technical Report 674, Department of Statistics, University of Wisconsin, Madison, WI.

# APPENDIX A
# CODE TO GENERATE EXAMPLE 2

```
% Cosine Demo [300 MHz]
%=========================================================================
% ELECTRIC FIELD: The 2-D plane-wave electric field
%
%   E(r) = [  sin(theta)  ]  cos(k'*r); k = [cos(theta)]
%          [ -cos(theta)  ]                 [sin(theta)]
%
% is sampled on the grid
%
%   0   < x < 1000
%   -100< y < 100
%
% If the carrier frequency is fC=300 MHz, the wavelength
%
%     lambda = c0/fC = 1    (m)
%
% and sets the wavenumber
%
%        k = 2*pi/lambda = 6.3
%
% COMPARISONS: This file compares the Gaussian spline to the
% linear and natural splines
%
% CODE AND COMPLAINTS
% jeffery.allen@navy.mil
%=========================================================================


% 1. RF "Measurements"

% 1.1 RF
fCMHz   = 300;          % Carrier frequency (MHz)
lambda  = 300/fCMHz;    % wavelength (m)
kW      = 2*pi/lambda;  % wavenumber
dx      = lambda/10;    % spatial sample increment
azDeg   = input('Enter azimuth of the electric field <15deg> ');
if isempty(azDeg); azDeg = 15; end
phi   = azDeg*pi/180;
uVec    = [cos(phi); sin(phi)];
kVec    = kW*uVec;
E0      = [0 1; -1 0]*uVec;

% 1.2 Fine meshing of the electric fields
xMax    = 10;
yMax    = 1;
xVec    = 0:dx:xMax;
yVec    = -yMax:dx:yMax;
[X,Y]   = meshgrid( xVec, yVec);
E1      = cos(kVec(1)*X + kVec(2)*Y ) * E0(1);
E2      = cos(kVec(1)*X + kVec(2)*Y ) * E0(2);


% 1.3 Report on the electric field
figure
subplot(2,1,1)
imagesc( xVec, yVec, E1 )
set(gca,'Ydir','normal')
ylabel('{\ity} (m)');
title([ '$E_1(\phi; {\bf r});  \phi$=' num2str(azDeg) ' deg'  ] ...
,'Interpreter','LaTeX');
hC = colorbar;
hC.Label.String = 'V/m';
caxis([-1 1])
subplot(2,1,2)
imagesc( xVec, yVec, E2 )
set(gca,'Ydir','normal')
xlabel('{\itx} (m)');
ylabel('{\ity} (m)');
title([ '$E_2(\phi; {\bf r}); f_C$=' num2str(fCMHz) ' MHz'  ] ...
,'Interpreter','LaTeX');
hC = colorbar;
hC.Label.String = 'V/m';
caxis([-1 1])
printOpt = input('Print the electric field <ret=no> ','s');
if ~isempty(printOpt)
    eval(['print -djpeg dfSpline_2DFit_-' int2str(azDeg) 'Deg_eField']);
end


% 2. Gaussian Spline

% 2.1 Select the interpolation points
Nx = length(xVec);
Ny = length(yVec);
Ni = input('Enter number of interpolation points <80> ');
if isempty(Ni); Ni=80; end
index =  unique(1 + floor( rand(Ni,2)*diag([Nx,Ny]) ), 'rows');
Ni = length(index);
disp(['Got ' num2str(Ni) ' unique points']);
IndX = index(:,1);
IndY = index(:,2);
xI = xVec(IndX);
yI = yVec(IndY);
```

```
% 2.2 Collect the interpolated E field
V = zeros(2,Ni);
for ni=1:Ni
    V(:,ni) = [E1(IndY(ni),IndX(ni)); E2(IndY(ni),IndX(ni)) ];
end


% 2.3 Display the sample points
figure
plot( xI , yI , 'o', 'MarkerFaceColor' ,'b')
shg
axis([0 10 -3 3])
grid
xlabel('{\itx} (m)');
ylabel('{\ity} (m)');
printOpt = input('Print the sample points <ret=no> ','s');
if ~isempty(printOpt)
    eval(['print -djpeg dfSpline_2DFit_' int2str(azDeg) 'Deg_' int2str(Ni) 'Samples']);
end


% 2.4 Display the sampled electric field
figure
e2I = zeros(Ni,1);
for ni=1:Ni
    e2I(ni) = E2(IndY(ni),IndX(ni));
end
stem3( xI, yI, e2I, 'filled' )
xlabel('{\itx} (m)');
ylabel('{\ity} (m)');


% 2.5 Spline analysis

% 2.5.1 % Set the spatial grating
gR = 1;

% 2.5.2 Analysis
W = dfSpline_2DAnalysis(gR,xI,yI,V);

% 2.5.3 Synthesis
[phi1,phi2] = dfSpline_2DSynthesis(gR,xI,yI,X,Y,W);

% 2.5.4 Report the Gaussian Spline
figure
subplot(2,1,1)
imagesc( xVec, yVec, phi1 )
set(gca,'Ydir','normal')
ylabel('{\ity} (m)');
title([ 'Gaussian Spline $\approx E_1(\phi; {\bf r}); \phi$=' num2str(azDeg) ' deg'  ] ...
,'Interpreter','LaTeX');
hC = colorbar;
hC.Label.String = 'V/m';
caxis([-1 1])
subplot(2,1,2)
imagesc( xVec, yVec, phi2 )
set(gca,'Ydir','normal')
xlabel(['{\itx} (m): {\itN_i}=' num2str(Ni) ' sample points; \beta=' num2str(gR) ]);
ylabel('{\ity} (m)');
title([ 'Gaussian Spline $\approx E_2(\phi; {\bf r});  f_C$=' num2str(fCMHz) ' MHz'  ] ...
,'Interpreter','LaTeX');
hC = colorbar;
hC.Label.String = 'V/m';
caxis([-1 1])
printOpt = input('Print the Gaussian spline <ret=no> ','s');
if ~isempty(printOpt)
    eval(['print -djpeg dfSpline_2DFit_' int2str(azDeg) 'Deg_' int2str(Ni) 'Samples_Gaussian']);
end


% 3. Linear spline
e1Spline = scatteredInterpolant( xI(:), yI(:), V(1,:)', 'linear' );
e1Linear = e1Spline(X,Y);
e2Spline = scatteredInterpolant( xI(:), yI(:), V(2,:)', 'linear');
e2Linear = e2Spline(X,Y);
figure
subplot(2,1,1)
imagesc( xVec, yVec, e1Linear )
set(gca,'Ydir','normal')
ylabel('{\ity} (m)');
title([ 'Linear Spline $\approx E_1(\phi; {\bf r}); \phi$=' num2str(azDeg) ' deg'  ] ...
,'Interpreter','LaTeX');
hC = colorbar;
hC.Label.String = 'V/m';
caxis([-1 1])
subplot(2,1,2)
imagesc( xVec, yVec, e2Linear )
set(gca,'Ydir','normal')
xlabel(['{\itx} (m): {\itN_i}=' num2str(Ni) ' sample points']);
ylabel('{\ity} (m)');
title([ 'Linear Spline $\approx E_2(\phi; {\bf r}); f_C$=' num2str(fCMHz) ' MHz'  ] ...
,'Interpreter','LaTeX');
hC = colorbar;
hC.Label.String = 'V/m';
caxis([-1 1])
printOpt = input('Print the linear spline <ret=no> ','s');
if ~isempty(printOpt)
    eval(['print -djpeg dfSpline_2DFit_' int2str(azDeg) 'Deg_' int2str(Ni) 'Samples_Linear']);
end
```

```
% 4. Natural spline
e1Spline = scatteredInterpolant( xI(:), yI(:), V(1,:)', 'natural' );
e1Nat    = e1Spline(X,Y);
e2Spline = scatteredInterpolant( xI(:), yI(:), V(2,:)', 'natural');
e2Nat    = e2Spline(X,Y);
figure
subplot(2,1,1)
imagesc( xVec, yVec, e1Nat )
set(gca,'Ydir','normal')
ylabel('{\ity} (m)');
title([ 'Natural Spline $\approx E_1(\phi; {\bf r}); \phi$=' num2str(azDeg) ' deg'  ] ...
,'Interpreter','LaTeX');
hC = colorbar;
hC.Label.String = 'V/m';
caxis([-1 1])
subplot(2,1,2)
imagesc( xVec, yVec, e2Nat )
set(gca,'Ydir','normal')
xlabel(['{\itx} (m): {\itN_i}=' num2str(Ni) ' sample points' ]);
ylabel('{\ity} (m)');
title([ 'Natural Spline $$\approx E_2(\phi; {\bf r}); f_C$=' num2str(fCMHz) ' MHz'  ] ...
,'Interpreter','LaTeX');
hC = colorbar;
hC.Label.String = 'V/m';
caxis([-1 1])
printOpt = input('Print the Natural spline <ret=no> ','s');
if ~isempty(printOpt)
    eval(['print -djpeg dfSpline_2DFit_' int2str(azDeg) 'Deg_' int2str(Ni) 'Samples_Natural']);
end
```

This page is intentionally blank.

# APPENDIX B
# 2-D GAUSSIAN SPLINE ANALYSIS CODE

```
function W = dfSpline_2DAnalysis(gR,xI,yI,V)
%==========================================================================
% This function computes the "analysis" of a 2-D electric field samples
%
%   {xI(n),yI(n),V(n)};  n=1:N
%
% using 2-D Gaussian splines. This analysis, like the wavelet analysis,
% finds the matrix 2-by-N matrix "W" that interpolates the electric field:
%
%           N
%   V(m) = sum  Phi(gR; xI(m) - xI(n), yI(m) - yI(n) )*W(:,n)
%          n=1
%
% and Phi(gR;x,y) is the 2-by-2 Gaussian matrix [1]:
%
%     Phi(gR; x,y) = 2*gR*exp( -gR*(x^2 + y^2) ) ...
%                  *  [ 1- 2*gR*y^2   2*gR*x*y     ]
%                     [ 2*gR*x*y      1 - 2*gR*x^2 ]
%
% REFERENCES
% [1] McNally, Colin P. [2011]
% Divergence-Free Interpolation of Vector Fields from Point
% Values---Exact $\nabla\cdot{\bf B}=0$ in Numerical Solutions,
% Mon. Not. R. Astron. Soc.
%
% CODING AND COMPLAINTS
% jeffery.allen@navy.mil
%==========================================================================

% 1. Number of interpolation points
Ni = length(xI);

% 2. Fill the Vandermode matrix
PHI = zeros( 2*Ni, 2*Ni );
for nr = 1:Ni

    % 2.1 Point to the row of PHI
    xr = xI(nr);
    yr = yI(nr);

    for nc = 1:Ni

        % 2.2 Point to the column of PHI
        xc = xI(nc);
        yc = yI(nc);

        % 2.3 Fill the (nr,nc) block of PHI
        [phi11, phi12, ...
         phi21, phi22] = dfSpline(gR,xr,yr,xc,yc);
        PHI( 2*(nr-1) + [0:1] + 1, 2*(nc-1) + [0:1] + 1) ...
        = [phi11, phi12;   ...
           phi21, phi22];

    end

end

% 3. Trim the tiny elements to avoid a full inversion
PHI( find(PHI)<10^-4 ) = [];
PHI = sparse(PHI);

% 4. Solve the nodal equation
W = reshape(PHI\V(:) , 2 ,Ni );

return
end
```

This page is intentionally blank.

# APPENDIX C
# 2-D GAUSSIAN SPLINE SYNTHESIS CODE

```
function [phi1,phi2] = dfSpline_2DSynthesis(gR,xI,yI,X,Y,W)
%==========================================================================
% This function computes the "synthesis" of a 2-D electric field from
% samples of the field
%
%   {xI(n),yI(n),V(n)};  n=1:N
%
% using 2-D Gaussian splines. This synthesis, like the wavelet synthesis,
% interpolates the electric field as
%
%             N
%   V(x,y) = sum  Phi(gR; x - xI(n), y - yI(n) )*W(:,n)
%            n=1
%
% where matrix 2-by-N matrix "W" is computed from the "analysis"
%
%             W = dfSpline_2DAnalysis(gR,xI,yI,V)
%
% and Phi(gR;x,y) is the 2-by-2 Gaussian matrix [1]:
%
%     Phi(gR; x,y) = 2*gR*exp( -gR*(x^2 + y^2) ) ...
%                  *  [ 1- 2*gR*y^2   2*gR*x*y     ]
%                     [ 2*gR*x*y      1 - 2*gR*x^2 ]
%
% REFERENCES
% [1] McNally, Colin P. [2011]
% Divergence-Free Interpolation of Vector Fields from Point
% Values---Exact $\nabla\cdot{\bf B}=0$ in Numerical Solutions,
% Mon. Not. R. Astron. Soc.
%
% CODING AND COMPLAINTS
% jeffery.allen@navy.mil
%==========================================================================


phi1 = 0;
phi2 = 0;
Ni   = length(xI);
for ni=1:Ni

    % 2.7.1 Nodal point
    xi = xI(ni);
    yi = yI(ni);

    % 2.7.2 Sample the node
    [ phi11,  phi12   ...
    , phi21,  phi22 ]  = dfSpline(gR,xi,yi,X,Y);

    % 2.7.3 Sum the nodes
    phi1 = phi1 +  phi11*W(1,ni) + phi12*W(2,ni);
    phi2 = phi2 +  phi21*W(1,ni) + phi22*W(2,ni);


end
return
end
```

This page is intentionally blank.

# APPENDIX D
# 2-D GAUSSIAN SPLINE CODE

```
function [phi11, phi21, phi12,phi22] = dfSpline(gR,x0,y0,X,Y,plotOpt)
%=========================================================================
% Computes the 2-by-2 Gaussian matrix [1]:
%
%     Phi(gR; x,y) = 2*gR*exp( -gR*(X^2 + Y^2) ) ...
%                  *  [ 1- 2*gR*Y^2   2*gR*X*Y     ]
%                     [ 2*gR*X*Y      1 - 2*gR*X^2 ]
% where
%                X = x  - x0
%                Y = y  - y0
%
% REFERENCES
% [1] McNally, Colin P. [2011]
% Divergence-Free Interpolation of Vector Fields from Point
% Values---Exact $\nabla\cdot{\bf B}=0$ in Numerical Solutions,
% Mon. Not. R. Astron. Soc.
%
% CODING AND COMPLAINTS
% jeffery.allen@navy.mil
%=========================================================================


if nargin < 6
    plotOpt = 0;
end
if nargin == 0
    x0      = 0;
    y0      = 0;
    gR      = 1/4;
    xVec    = linspace(-2.5,2.5,31);
    yVec    = linspace(-3.5,3.5,33);
    [X,Y]   = meshgrid( xVec, yVec);
    plotOpt = 1;
end

X0  = X - x0;
Y0  = Y - y0;

phi   = exp( -gR*(X0.^2 + Y0.^2) );

phi11 = 2*gR*phi.*( 1 - 2*gR*Y0.^2 );
phi21 = 4*gR^2*phi.*X0.*Y0;
phi12 = phi21;
phi22 = 2*gR*phi.*( 1 - 2*gR*X0.^2 );


if nargin == 0 || plotOpt == 1
    figure
    quiver(X,Y,phi11,phi21);
    ylabel('{\ity}');
    xlabel('{\itx}');
    title(['\Phi(:,1): {\itg_R}=' num2str(gR)] );

    figure
    surfl(X,Y, sqrt( phi11.^2 + phi21.^2 ) );
    colormap copper
```

```
    shading interp
    ylabel('{\ity}');
    xlabel('{\itx}');
    title(['||\Phi(:,1): {\itg_R}=' num2str(gR)] );

    figure
    quiver(X,Y,phi12,phi22);
    ylabel('{\ity}');
    xlabel('{\itx}' );
    title(['\Phi(:,2): {\itg_R}=' num2str(gR)] );

     figure
    surfl(X,Y, sqrt( phi12.^2 + phi22.^2 ) );
    colormap copper
    shading interp
    ylabel('{\ity}');
    xlabel('{\itx}');
    title(['||\Phi(:,2)||: {\itg_R}=' num2str(gR)] );
end
```

# INITIAL DISTRIBUTION

| | | |
|---|---|---|
| 84310 | Technical Library/Archives | (1) |
| 75250 | J. C. Allen | (1) |
| 52270 | D. R. Hilton | (1) |
| 52270 | K. R. Buchanan | (1) |
| 52250 | J. H. Meloling | (1) |

Defense Technical Information Center
Fort Belvoir, VA 22060–6218 (1)

Chief of Naval Operations for Information
Dominance/Director of Naval Intelligence
(OPNAV N2/N6) (1)

This page is intentionally blank.

# REPORT DOCUMENTATION PAGE

*Form Approved*
*OMB No. 0704-01-0188*



**PLEASE DO NOT RETURN YOUR FORM TO THE ABOVE ADDRESS.**

| 1. REPORT DATE *(DD-MM-YYYY)* | 2. REPORT TYPE | 3. DATES COVERED *(From - To)* |
|---|---|---|
| April 2021 | Technical Report | |

**4. TITLE AND SUBTITLE**

Physics-Based Splines Interpolating Electric-Field Measurements.

**5a. CONTRACT NUMBER**

**5b. GRANT NUMBER**

**5c. PROGRAM ELEMENT NUMBER**

**5d. PROJECT NUMBER**

**5e. TASK NUMBER**

**5f. WORK UNIT NUMBER**

**6. AUTHORS**

Jeffery C. Allen
David R. Hilton
Kristopher R. Buchanan
John H. Meloling
**NIWC Pacific**

**7. PERFORMING ORGANIZATION NAME(S) AND ADDRESS(ES)**

NIWC Pacific
53560 Hull Street
San Diego, CA 92152–5001

**8. PERFORMING ORGANIZATION REPORT NUMBER**

TR-3232

**9. SPONSORING/MONITORING AGENCY NAME(S) AND ADDRESS(ES)**

Evangela M. Waite
1333 Isaac Hull Ave
SE BLDG 197R , Washington Navy Yard, DC, 20376-0005

**10. SPONSOR/MONITOR'S ACRONYM(S)**

Part of NAVSEA 05H

**11. SPONSOR/MONITOR'S REPORT NUMBER(S)**

**12. DISTRIBUTION/AVAILABILITY STATEMENT**

DISTRIBUTION STATEMENT A: Approved for public release.

**13. SUPPLEMENTARY NOTES**



**14. ABSTRACT**

Mitigating Electro-Magnetic Interference (EMI) is a long-term engineering problem for shipboard RF systems [15], [14]. Measuring the electric field is basic to EMI mitigation. This report analyses electric-field measurements taken on the flight deck of a carrier. These electric field is sparsely sampled at selected locations on the flight deck. Interpolation schemes "fill in" the electric field between sample points. The quality of these interpolated electric fields is the "object of discussion" of this report. Standard splines do not encode the physics of the problem—that the electric field in free space has zero divergence. This report develops a class of splines with zero divergence. Comparisons between these divergence-free splines and standard splines demonstrates enforcing zero divergence improves the quality of the spline—fewer sample points are required to recover the electric field with greater accuracy than the standard splines. Applying a divergence-free spline to these flight-deck measurements requires a hybrid approach because only the electric field magnitude was measured. The hybrid approach exploits knowledge of the physical measurement to constrain the divergence-free splines to interpolate the amplitude at each sample point while leaving the phases as free variables at each sample point. The phases are optimized to approximate the splined electric-field magnitude. Consequently, the hybrid approach produces a divergence-free spline that matches the measured amplitude at each sample point and is a best approximation to the standard spline.

**15. SUBJECT TERMS**

Physics-Based Spline; Interpolating Electric-Field Measurements; EMI mitigation; 3-D electric field

| 16. SECURITY CLASSIFICATION OF: | | | 17. LIMITATION OF ABSTRACT | 18. NUMBER OF PAGES | 19a. NAME OF RESPONSIBLE PERSON |
|---|---|---|---|---|---|
| a. REPORT | b. ABSTRACT | c. THIS PAGE | | | Jeffery C. Allen |
| U | U | U | SAR | 80 | 19B. TELEPHONE NUMBER *(Include area code)* (619) 553-6566 |

This page is intentionally blank.

This page is intentionally blank.


Naval Information Warfare Center Pacific (NIWC Pacific)
San Diego, CA 92152-5001